Abschlussbericht

Teilvorhaben: Experimentelle und theoretische Untersuchungen zu Materialien und neuen Bauelementkonzepten der Silizium Photonik

Verbundprojekt: Neuartige Lichtquellen und Komponenten für Silizium-Photonik (SiliconLight)

Zuwendungsempfänger: Technische Hochschule Wildau (FH)

Förderkennzeichen: 13N9734

Laufzeit des Vorhabens: 01.06.2008 – 31.05.2011

Teil I: Zusammenfassung

1) Aufzählung der wichtigsten wissenschaftlich-technischen Ergebnisse und anderer wesentlicher Ereignisse.

- A theoretical analysis of the Raman scattering asymmetry in silicon crystal was carried out. The effect of scattering geometry on conversion efficiency as well on the polarization state of output radiation was investigated.
- A theoretical model for description of stimulated Raman scattering in bulk silicon was developed. The model considers both single- or multi-pass Raman generation and Raman lasing. Using this model a theoretical investigation of Raman conversion in bulk silicon was carried out. Conditions for Raman threshold were determined. Numerical calculation and optimization of Raman conversion efficiency was performed.
- Simulation of Raman conversion of Raman laser operating at temperature of 10 K was performed. A theoretical model developed for this purpose involves a calculation of free-carriers induced lens. Results of performed simulations are in a good quantitative agreement with experimental results performed by the project partner TUB. The results of calculations show a strong effect of a negative free-carrier lens, which leads to a shortening of the Raman interaction length. It is also shown theoretically that a 1.5 times increase of pump beam diameter results in a 2.5 times increase of Stokes output energy.
- A theoretical model for description of Raman conversion in a SOI-based ring Raman laser was developed. An investigation of Raman threshold condition was performed. Optimal parameters of Raman cavity length and coupling ratios of the coupler of this laser at pump and Stokes wavelengths were determined.
- A design of waveguide geometry was carried out using Finite Elements Analysis. The design allowed the creation of the waveguide for a Raman ring laser with defined values of coupling ratios for pump and Stokes wavelengths. The designed integrated structures were realized on chip and investigated by optical techniques.

- Numerical simulation and design of electric contacts for electro-optical modulators were performed. A contact structure consisting of a transmission part, a matching line, and an active element, was considered. The transmission part impedance was calculated analytically to be 47 Ohms, what means a good matching with standard 50 Ohms coaxial cables. Impedance of the active element and the matching line was calculated numerically using Finite Elements Analysis. Ways for further optimization of impedance matching are shown.
- Synthesis and preparation of polymeric materials for second order nonlinear optical applications have been carried out with the aim to develop electro-optical modulators especially for fabrication of electric tunable Fabry-Perot filters. Materials with very good film forming properties have been obtained which can be used for fabrication of such electro-optic devices.

2) Vergleich des Stands des Vorhabens mit der ursprünglichen (bzw. mit Zustimmung des ZG geänderten) Arbeits-, Zeit- und Kostenplanung.

☒* Das Vorhaben liegt im Wesentlichen innerhalb der ursprünglichen (bzw. mit Zustimmung des ZG geänderten) Arbeits-, Zeit- und Kostenplanung.
☐* Eine Anpassung des Arbeitsplans wird erforderlich (Erläuterung erforderlich).
☐* Es sind zeitliche Verzögerungen aufgetreten (Erläuterung erforderlich).
☐* Es sind Mehr- oder Minderausgaben aufgetreten (Erläuterung erforderlich).

3) Haben sich die Aussichten für das Erreichen der Ziele des Vorhabens innerhalb des angegebenen Berichtszeitraums gegenüber dem ursprünglichen Antrag geändert (Begründung)?

☒* Die Aussichten für das Erreichen der Ziele des Vorhabens haben sich gegenüber dem Zeitpunkt der Antragstellung nicht verändert.
☐* Die Aussichten für das Erreichen der Ziele des Vorhabens haben sich geändert (Erläuterung erforderlich).

4) Sind inzwischen von dritter Seite FuE-Ergebnisse bekannt geworden, die für die Durchführung des Vorhabens relevant sind?

☒* Nein
☐* Ja (Erläuterung erforderlich)

5) Sind oder werden Änderungen in der Zielsetzung notwendig?

☒* Nein
☐* Ja (Erläuterung erforderlich)

6) Jährliche Fortschreibung des Verwertungsplans. Diese soll, soweit im Einzelfall zutreffend, Angaben zu folgenden Punkten enthalten:

---

* Bitte ggf. per Doppelklick aktivieren.   Stand 30.11.2009

* Bitte ggf. per Doppelklick aktivieren.   Stand: 30.11.2009

☒* Im Berichtszeitraum wurden auf Basis der Ergebnisse des Vorhabens Schutzrechte angemeldet, erteilt oder eine Anmeldung vorbereitet (Erläuterung erforderlich).

☐* Im Berichtszeitraum sind Änderungen der wirtschaftlichen Erfolgsaussichten nach Projektende gegenüber der Darstellung im Antrag aufgetreten (Erläuterung erforderlich).

☐* Im Berichtszeitraum sind Änderungen der wissenschaftlichen und/oder technischen Erfolgsaussichten nach Projektende gegenüber der Darstellung im Antrag aufgetreten (Erläuterung erforderlich).

☐* Im Berichtszeitraum sind Änderungen der wissenschaftlichen und wirtschaftlichen Anschlussfähigkeit gegenüber der Darstellung im Antrag aufgetreten (Erläuterung erforderlich).

Teil II: Ausführlicher Sachbericht

The works during the project were carried out in the three working-areas. These are

1) LEDs in CMOS-compatible silicon based technology *("LEDs in CMOS kompatibler Siliziumtechnologie")*;

2) silicon Raman laser (*"Silizium-Ramanlaser"*);

3) passive- and active- waveguide structures (*"Passive/active Wellenleiterstrukturen, incl. Modulatoren"*).

The activity for TH Wildau was organized in eight work-packages. Three work-packages (AP2 *„Aufklärung der Ladungstransportparameter und Emissionscharaktersitika von MIS-LEDs mit Band-Band-Emission bei λ = 1,1 µm auf Bulk-Si und SOI"*, AP3 *„Aufklärung der Ladungstransportparameter und Emissionscharaktersitika von MIS-LED mit λ ~ 1,5 µm unter Nutzung von Versetzungsnetzwerken auf Bulk-Material"*, and AP4 *„Charakterisierung von MIS-LED mit λ ~ 1,5 µm unter Nutzung von Versetzungsnetzwerken auf SOI"*) corresponded to the first working-area. Both theoretical and experimental investigations of MIS-LED structures were planned in the frame of these work-packages. One work-package (AP5 *"Modellierung von Raman-Laser Resonatoren für Silizium-Bulk und SOI Wellenleiter"*) corresponded to the second working-area, devoted to the design and development of silicon Raman laser. Three work-packages (AP6 *"Charakterisierung von SOI-Wellenleiterstrukturen für Modulatoren und Raman-Laser"*, AP7 *„Polymere für planare Fabry-Perot Modulatoren (in Hybrid-Technologie)"*, and AP8 *„Wellenleiterintegration"*) corresponded to the third working-area. Finally, one work-package (AP1 *"Projektkoordination"*) was devoted to the coordination of activity of all project participants.

Unfortunately, due to the withdrawal of one project participant (MergeOptics GmbH) from the project, the planned tasks had to be redistributed between the remaining participants. As a result tasks of TH Wildau in the first working-area were transferred to the partner IHP/Joint Lab BTU-IHP. In return TH Wildau got the following tasks of MergOptics GmbH: *"Modulator in SOI-Wellenleiterstrukturen mit verspiegelten Facetten"*, *"Design, Herstellung und Test von planaren Fabry-Perot Modulatoren (in Hybrid-Technologie)"*, and *"Raman-Laser in SOI-Wellenleiterstrukturen mit verspiegelten Facetten"*, which were carried out in the frame of work-packages AP5, AP6, and AP7, respectively. So, main effort was concentrated in the second working-area (work-

package AP5), the third working-area (work-packages AP6, AP7 and AP8), and in the project coordination (work-package AP1). Main tasks here were the following:

- investigation of effect of crystal orientation of silicon on stimulated Raman scattering (SRS);
- modeling of Raman converters based on bulk-silicon;
- modeling of Raman converters based on SOI-waveguide;
- design of SOI-waveguide structure for Raman laser and modulators;
- modeling and optimization of electrical contacts for high-frequency electro-optical modulators (both polymer- and SOI-waveguide based);
- production, poling and characterization of polymer materials for the use in electro-optical modulators based on plane Fabry-Perot resonators

The main scientific and technical results obtained during the fulfillment of these tasks are presented in detail in the following chapters.

II.1 Theoretical investigation of stimulated Raman scattering in Bulk-Silicon

Various aspects of SRS in silicon bulk crystal were considered. This involves, in particular, an effect of orientation of the crystal with respect to propagation direction and polarization of the pump beam on Raman conversion efficiency and polarization state of converted Stokes radiation. Also conditions for Raman threshold as well as possible achievable efficiencies were determined for bulk silicon both for single-pass SRS and Raman laser scheme.

II.1.1 Crystal orientation

The silicon crystal has diamond structure, i.e. two identical face centered cubic (fcc) structures shifted against each other by a quarter of the primitive lattice vectors along all three spatial directions. Though the silicon crystal has a cubic symmetry like barium nitrate crystal its ability for Raman conversion is anisotropic. An intense Raman active optical mode of silicon with a frequency of 521 cm^{-1} [1] corresponds to a threefold degenerated lattice vibration F_{2g}. In contrast to A-vibrations, which are active in conventional Raman crystals like barium nitrate or potassium gadolinium tungstate, and which show an isotropic scattering behavior in cubic crystals, the scattering matrix of the F-vibration depends on the direction of observation. This means that the Raman efficiency depends on the scattering geometry and calculation of an optimal geometry is of special importance.

If the directions of pump and Stokes waves are identical (forward scattering) and coincide with the cubic axis [100] of the crystal the scattering matrix has the following form [2]:

$$F_{100} = \begin{pmatrix} 6 & 0 & 0 & 0 \\ 0 & -6 & 0 & 0 \\ 0 & 0 & 6 & 0 \\ 0 & 0 & 0 & -6 \end{pmatrix}. \tag{1}$$

For scattering along the dodecahedral [110] and octahedral [111] axes the scattering matrices are

$$F_{110} = \begin{pmatrix} 9 & 3 & 0 & 0 \\ 3 & -3 & 0 & 0 \\ 0 & 0 & 6 & 0 \\ 0 & 0 & 0 & -6 \end{pmatrix} \tag{2}$$

and

$$F_{111} = \begin{pmatrix} 10 & 0 & 0 & 0 \\ 0 & 2 & 0 & 0 \\ 0 & 0 & 2 & 0 \\ 0 & 0 & 0 & -6 \end{pmatrix}. \tag{3}$$

The scattering matrix describes how the polarization states of incoming and outgoing beams expressed by the so-called Stokes parameters are related to each other within the scattering process. Stokes parameters are usually written in the form of a four-component vector [3]:

$$\begin{pmatrix} I \\ P_1 \\ P_2 \\ P_3 \end{pmatrix} = \begin{pmatrix} I \\ P \end{pmatrix}, \tag{4}$$

where I is the total intensity of the beam under consideration, P_1 describes the presence of a linear polarization with respect to a characteristic crystallographic reference plane (TE or TM), P_2 describes a linear polarization at an angle of $\pi/4$ to the right with respect

6

to the reference plane, and P_3 describes the presence of circular polarization ("+1" for a left circular polarization, and "-1" for a right circular polarization).

The Stokes parameters of scattered radiation can be calculated using following equation:

$$\begin{pmatrix} I' \\ P' \end{pmatrix} = M \begin{pmatrix} I \\ P \end{pmatrix}, \tag{5}$$

where M is the scattering matrix, I' and P' are intensity and polarization three-vectors of the scattered radiation, respectively.

Using equation (5) and matrices (1) to (3), we calculated the Stokes parameters of scattered radiation for backward Raman scattering along the corresponding axes. It was found that the intensity of the scattered signal along the [100] axis does not depend on the polarization state of pump radiation. Linearly polarized light is scattered into linearly polarized one, while non-polarized light is scattered into non-polarized one. It should be noted that the polarization of the pump signal is perpendicular to the scattered signal.

The intensity of a signal scattered along the [111] axis does also not depend on pump beam polarization. The polarization state of the scattered light is in this case identical to the polarization state of pump radiation.

Scattering along the [110] axis is more complicated. The intensity depends on the polarization state of pump radiation against a reference plane. Scattering of vertically polarized light is two times stronger than that of horizontally polarized light. In addition, vertically polarized pump radiation produces completely non-polarized scattered radiation, while horizontally polarized pump radiation scatters into vertically polarized light.

The highest intensity of scattered radiation is obtained for a pump beam directed along the [110] axis. The intensities of radiation scattered along the axes [111] and [100] are 17% and 50% lower, respectively. The advantage of these orientations is that efficiency does not depend on the polarization of light, what simplifies the exploitation of Si-crystals cut at any of these orientations. The dependence of the Raman efficiency was experimentally verified by another project participant, TUB. Good correspondence between modeling and experimental results was observed.

II.1.2 Calculation of Raman conversion in bulk silicon (single-pass scheme)

For calculation of SRS in bulk silicon in single-pass scheme we considered a forward SRS in steady-state regime, when the coherence time of the pump pulse is much longer than the dephasing time of the Raman vibration. This assumption is correct if the pump spectral bandwidth is smaller than the spectral bandwidth of the Raman line (106 GHz = 3.5 cm^{-1} [4]). In this case the interaction of pump and Stokes waves in the traveling coordinate system can be described with following equations [5, 6]:

$$\frac{\partial}{\partial z} I_P(t,z) = -\beta \cdot \left((I_P)^2 + 2 I_P I_S \right) - \frac{v_P}{v_S} g I_P I_S - \sigma_P Q I_P, \tag{6}$$

$$\frac{\partial}{\partial z} I_S(t,z) = -\beta \cdot \left((I_S)^2 + 2 I_P I_S \right) + g I_S I_P - \sigma_S Q I_S, \tag{7}$$

$$Q(t,z)'_t = -\frac{1}{t_{FC}} Q + \beta \cdot \left(\frac{(I_P)^2}{2hv_P} + \frac{(I_S)^2}{2hv_S} + \frac{4 I_P I_S}{h \cdot (v_P + v_S)} \right), \tag{8}$$

where $I_P(t,z)$ and $I_S(t,z)$ are intensities of pump and Stokes waves, $Q(t,z)$ is the concentration of free-carriers induced via two-photon absorption, β is the two-photon absorption coefficient, σ_S and σ_P are cross-sections for free-carrier absorption at Stokes and pump wavelengths, respectively, h is Plank's constant, v_P and v_S are pump and Stokes frequencies, respectively, c is speed of light, g is the Raman gain coefficient, t_{FC} is the life time of free-carriers, α_{SP} is the coefficient of spontaneous scattering.

Numerical solution of equations (6)-(8) was performed for a pump wavelength of 1341 nm. The corresponding first Stokes wavelength is 1442 nm. The following values for the model parameters were used: β = 0.5 cm/GW [7], σ_P = 1.09×10^{-17} cm^2, σ_S = 1.25×10^{-17} cm^2 [5], t_C = 1 µs [8]. Unfortunately, the value of the Raman gain coefficient for silicon at a wavelength of 1341 nm is not exactly known. So we used values from 10 to 40 cm/GW in our calculations to estimate the resulting threshold. These values are in a good agreement with those used in the literature [4, 6, 7, 9-12].

Calculation of Raman threshold

At threshold condition the equation set (6)-(8) can be simplified. In that case the Stokes intensity is sufficiently smaller than the pump intensity:

$$I_P \gg I_S. \tag{9}$$

This allows the following simplification of the set of equations (6)-(8) [5, 7]:

$$\frac{\partial}{\partial z} I_P(t,z) = -\beta \cdot I_P^2 - \sigma_P Q I_P, \tag{10}$$

$$\frac{\partial}{\partial z} I_S(t,z) = (g - 2\beta) I_S I_P - \sigma_S Q I_S, \tag{11}$$

$$Q(t,z)'_t = -\frac{1}{t_{FC}} Q + \beta \frac{I_P^2}{2h\nu_P}. \tag{12}$$

The solution of equation (11) can be found in the following form:

$$I_S(t,z) = I_{S0} \exp\left(\int_0^z \left((g - 2\beta) I_P(t,z') - \sigma_S Q(t,z') \right) dz' \right), \tag{13}$$

where I_{S0} is the intensity of quantum noise at Stokes wavelength.

The Raman threshold occurs when the exponent in Eq.(13) is nearly equal to 25:

$$G_S(t) = \int_0^{L_{CR}} \left((g - 2\beta) I_P(t,z) - \sigma_S Q(t,z) \right) dz \approx 25, \tag{14}$$

where L_{CR} is the crystal length.

We used condition (14) together with equations (10) and (12) to determine the threshold of the pump radiation. The threshold is reached and Raman conversion starts if at any moment the value of $G_S(t)$ is equal to or higher then 25. The pump pulse is assumed as a Gaussian one in time:

$$I_P(t,r)\big|_{z=0} = \frac{J_P}{\sqrt{\pi} t_0} \exp\left(-t^2 / t_0^2 \right), \tag{15}$$

where $t_0 = \dfrac{t_{FWHM}}{2\sqrt{\ln 2}}$, t_{FWHM} is the pump pulse duration (full width at half maximum), J_P is the pump energy density.

Figure II.1.2.1a shows the dependence of threshold energy density on interaction length, calculated for a pulse duration of 200 ps and different values of the Raman gain coefficient. It can be seen that even for a value of Raman gain coefficient equal to 10 cm/GW, Raman threshold is possible for pump energy density less than 10 J/cm^2 if the interaction length is higher than 10 cm. For a value of the Raman gain coefficient of

40 cm/GW, threshold occurs at an energy density of 1 J/cm^2 for an interaction length of about 1 cm.
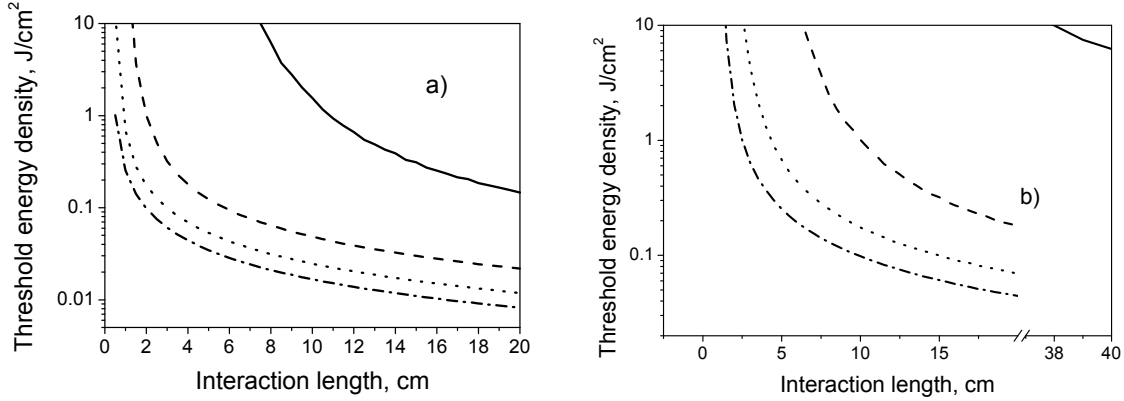

Figure II.1.2.1: Dependence of threshold energy density on interaction length calculated for pump pulse duration (a) of 200 ps and (b) of 1 ns, and for following values of Raman gain coefficient: 10 cm/GW (solid line), 20 cm/GW (dashed line), 30 cm/GW (dotted line), and 40 cm/GW (dash-dotted line).

The dependencies of threshold energy density on interaction length, calculated for pulse duration of 1 ns are presented in Figure II.1.2.1b. It can be seen that in this case a higher interaction length and energy density are required to reach the Raman threshold. For instance, for a Raman gain coefficient of 40 cm/GW the threshold energy density of 1 J/cm^2 corresponds to a length of about 2.5 cm. A Raman gain coefficient of 10 cm/GW requires an interaction length of 38 cm and higher to reach the threshold at an energy density of 10 J/cm^2. It should be noted that, due to the effect of TPA and FCA, a high enough interaction length is of special importance for reaching of Raman threshold in silicon. In usual Raman crystals, where there are no additional strong nonlinear effects like TPA and FCA, threshold intensity ($I_{Threshold}$) and threshold energy density ($J_{Threshold}$) are inversely proportional to the interaction length:

$$J_{Threshold} \sim I_{Threshold} = \frac{25}{g \cdot L_{CR}} \, .$$

(16)

Equation (16) means that the product of threshold energy density and interaction length is a constant and the decrease of interaction length can be compensated with proportional increase of threshold density. Figure II.1.2.2 presents the dependencies of $J_{Threshold} \times L_{CR}$ on interaction length calculated for a 1 ns pump pulse. It can be seen, that this product is not a constant but increases extremely when the interaction length decreases. Hence, the interaction length should be as high as possible. It should be

10

noted, that a high interaction length can be achieved by exploitation of multi-pass schemes (see Figure II.1.2.3), i.e. when the pump beam passes the Raman medium several times increasing, thus, the interaction length.
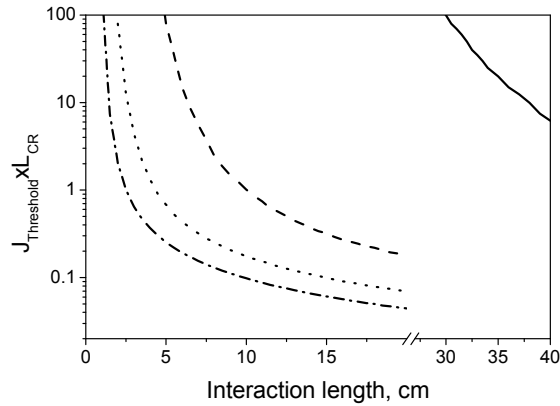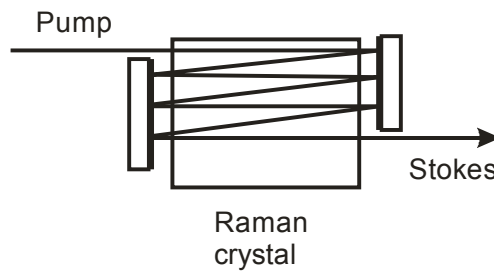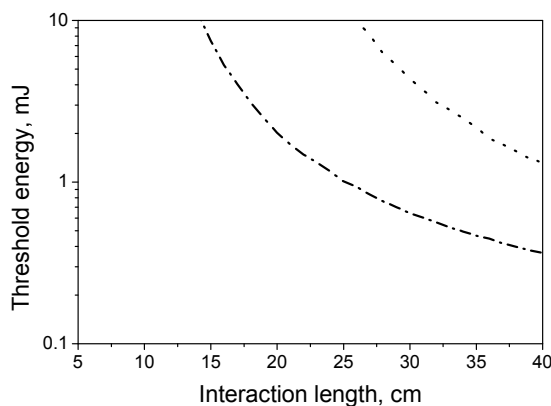

Figure II.1.2.2: The dependencies of $J_{Threshold} \times L_{CR}$ on interaction length calculated for pump pulse duration of 1 ns and for following values of Raman gain coefficient: 10 cm/GW (solid line), 20 cm/GW (dashed line), 30 cm/GW (dotted line), and 40 cm/GW (dash-dotted line).

Figure II.1.2.3: Scheme of multi-pass Raman generation.

Figure II.1.2.4: The dependencies of threshold energy density on interaction length calculated for pump pulse duration of 10 ns, and for following values of Raman gain coefficient: 30 cm/GW (dotted line), and 40 cm/GW (dash-dotted line).

Figure II.1.2.4 presents the dependencies of threshold energy density on interaction length, calculated for pulse duration of 10 ns. It can be seen that the threshold can be reached only if the Raman gain coefficient is higher than 30 cm/GW. Also a long interaction is required even for 40 cm/GW of Raman gain coefficient.

Hence, single-pass Raman threshold in bulk silicon is easily available for pumping with 200 ps pulses. For pump pulse duration of 1 ns the threshold also can be reached. However, for Raman gain coefficient of 10 cm/GW a high interaction length is required. For pumping with 10 ns pulses single-pass Raman threshold can be achieved only for Raman gain coefficients higher than 30 cm/GW.

Calculation of conversion efficiency

To calculate the Raman conversion efficiency and output Stokes energy it was necessary to take into account pump depletion and to solve the set of equations (6)-(8). We considered a pump beam with Gaussian spatial profile and supposed that each part of the beam is converted independently into Stokes radiation. Diffraction was not taken into account. This assumption is correct if the Fresnel number (F) is sufficiently higher than 1 [13]:

$$F = \frac{r_0^2}{\lambda_P L_{CR}} >> 1,\tag{17}$$

with λ_P – pump wavelength, r_0 – pump beam radius at $1/e^2$ level.

The pump energy density can be represented as follows:

$$J_P(r) = \frac{2}{\pi r_0^2} E_P \exp\left(-2 \frac{r^2}{r_0^2}\right),\tag{18}$$

with E_P - pump energy.

Solving equations (6)-(8) we obtain the efficiency of conversion (η_J) of pump energy density into Stokes energy density. The Stokes output energy (E_S) is calculated using the following expression:

$$E_S = \int_0^\infty \eta_J\left(J_P(r)\right) \cdot J_P(r) \cdot 2\pi r \cdot dr.\tag{19}$$
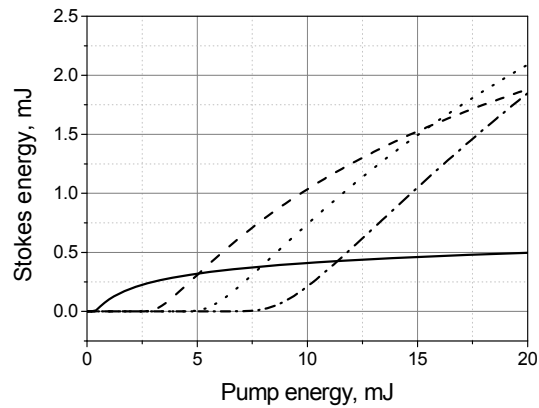
Figure II.1.2.5: The dependencies of the Stokes pulse energy on pump energy, calculated for pump pulse duration of 200 ps, Raman gain coefficient of 40 cm/GW, and interaction length of 3 cm; pump beam diameter is 1 mm (solid-line), 3 mm (dashed line), 4 mm (dotted line), and 5 mm (dash-dotted line).
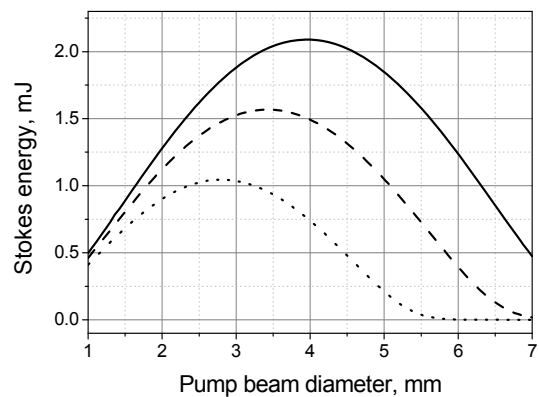

Figure II.1.2.6: Dependence of Stokes pulse energy on pump beam diameter, calculated for a pump pulse duration of 200 ps, Raman gain coefficient of 40 cm/GW, and interaction length of 3 cm; pump energy is 20 mJ (solid-line), 15 mJ (dashed line), and 10 mJ (dotted line).

Figure II.1.2.5 shows the dependencies of the Stokes pulse energy on pump energy, calculated for different values of pump beam diameter. Other parameters for this figure are the following: pump pulse duration is 200 ps, Raman gain coefficient is 40 cm/GW, interaction length is 3 cm. It can be seen, that the choice of pump beam diameter is important. Figure II.1.2.6 demonstrates the dependence of Stokes energy on the beam diameter. It shows that an optimal value of beam diameter exists. The decrease of pump beam diameter leads to an increase of pump intensity. This means low Raman threshold but strong pump depletion also due to nonlinear nature of TPA and FCA. An increase of pump beam diameter suppresses the influence of TPA and FCA, but increases the Raman threshold. Figure II.1.2.6 also shows that an optimal value of

beam diameter depends on pump energy. For instance, for pump energy of 20 mJ an optimal diameter is about 4 mm. This diameter provides a Stokes energy of nearly 2.1 mJ and a conversion efficiency of 10 %.

Figure II.1.2.7 presents the output Stokes energy versus pump energy calculated for different values of Raman gain coefficient. For each value of Raman gain coefficient an optimization of pump beam diameter was performed to provide maximum output energy at pump energy of 20 mJ. It can be seen, that the output energy depends strongly on the Raman gain coefficient. For Raman gain coefficient of 10 cm/GW the maximal output energy was only 0.4 µJ. Hence, the dependence for this small value of Raman gain coefficient is not shown in Figure II.1.2.7. For a Raman gain coefficient of 40 cm/GW the output energy is up to 3.8 mJ at a conversion efficiency of 19 %. It should be noted, that the curves presented in Figure II.1.2.7 have the same threshold energy in spite of different values of Raman gain. This is explained with the difference of beam diameters for these curves. An optimal pump beam diameter is larger for larger values of Raman gain coefficient providing lower threshold energy density as it was discussed in the previous section.
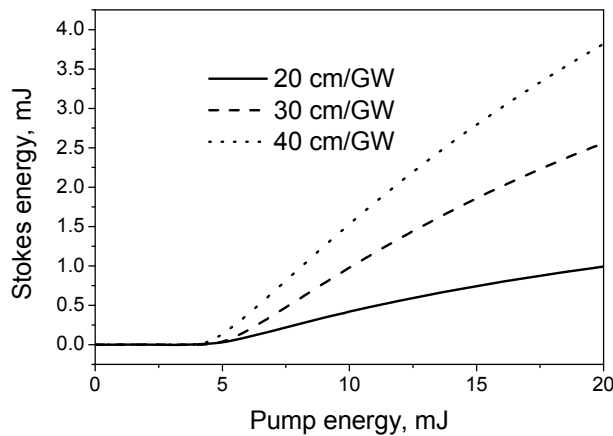

Figure II.1.2.7: Dependencies of Stokes energy on pump energy calculated for pump pulse duration of 200 ps, interaction length of 10 cm, and following values of Raman gain coefficient: 20 cm/GW (solid line), 30 cm/GW (dashed line), and 40 cm/GW (dotted line); pump beam diameters were optimized at maximum pump energy and were equal to 4 mm, 6 mm, and 7 mm, correspondingly.
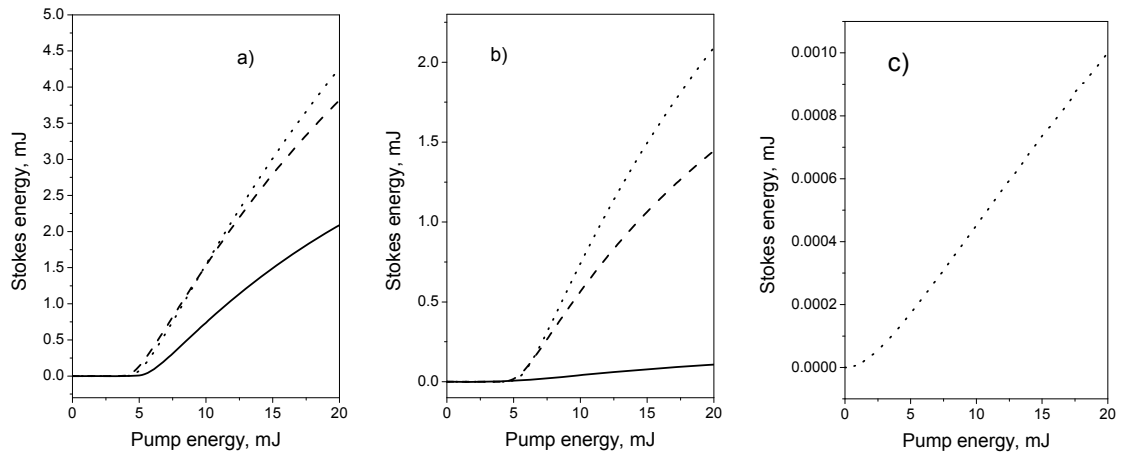
Figure II.1.2.8: The dependencies of output Stokes energy on pump energy calculated for interaction lengths of 3 cm (solid-line), 10 cm (dashed line), 15 cm (dotted line); Raman gain coefficient is 40 cm/GW, pump pulse duration is (a) 0.2 ns, (b) 1 ns, and (c) 10 ns.

The dependencies of output Stokes energy on pump energy calculated for interaction lengths of 3 cm, 10 cm, and 15 cm are presented in Figure II.1.2.8a. The Raman gain coefficient was taken to be 40 cm/GW. The pump beam diameter was optimized to provide highest efficiency at maximal pump energy and was equal to 4 mm, 7 mm, and 9 mm, respectively. It can be seen, that the increase of interaction length leads to an increase of output energy, but this increase is not very high. A five-fold increase of length leads to a doubling of Stokes energy.

The increase of pump pulse duration decreases energy and efficiency of Stokes pulses. Figures II.1.2.8b and II.1.2.8c show the dependencies of Stokes pulse energy on pump energy calculated for pump pulse durations of 1 ns and 10 ns, respectively. A value of Raman gain equal to 40 cm/GW was assumed. The pump beam diameter was also optimized for every curve. For a pump pulse duration of 1 ns the pump beam diameter was equal to 0.9 mm, to 3 mm, and to 4 mm for interaction length of 3 cm, 10 cm, and 15 cm, respectively. For a pump pulse duration of 10 ns only the curve for an interaction length of 15 cm is presented in Figure II.1.2.8c. An optimal pump beam diameter was equal to 0.16 mm. Figures II.1.2.8 show that the increase of pump pulse duration from 0.2 ns to 1 ns leads to about a two-fold decrease of generation efficiency. The increase of pump duration up to 10 ns resulted in formidable fall of the efficiency. For the curve presented in Figure II.1.2.8c the Stokes generation efficiency is only 5×10^{-3} %.

II.1.3 Calculation of Raman conversion in Bulk-Si (Raman laser)

As it is shown in the previous chapter the single-pass generation in silicon is ineffective for pump pulses with duration of ten and more nanoseconds. For this case, a silicon Raman laser can be involved, which allows a threshold decrease if pump pulse duration is sufficiently higher than the single-pass trip time. The possibility of silicon-based Raman laser realization was investigated.

For Raman lasing the propagation of pump and Stokes wave both in forward and backward directions should be considered [5, 7, 14]:

$$\left(\frac{\partial}{\partial z}+\frac{1}{c}\frac{\partial}{\partial t}\right)I_P^f(t,z)=-\beta\cdot\left(\left(I_P^f\right)^2+2I_P^fI_P^b+2I_P^fI_S^f+2I_P^fI_S^b\right)- $$
$$-\frac{v_P}{v_S}gI_P^f\cdot\left(I_S^f+I_S^b\right)-\sigma_PQI_P^f \qquad (20)$$

$$\left(-\frac{\partial}{\partial z}+\frac{1}{c}\frac{\partial}{\partial t}\right)I_P^b(t,z)=-\beta\cdot\left(\left(I_P^b\right)^2+2I_P^bI_P^f+2I_P^bI_S^f+2I_P^bI_S^b\right)- $$
$$-\frac{v_P}{v_S}gI_P^b\cdot\left(I_S^f+I_S^b\right)-\sigma_PQI_P^b \qquad (21)$$

$$\left(\frac{\partial}{\partial z}+\frac{1}{c}\frac{\partial}{\partial t}\right)I_S^f(t,z)=-\beta\cdot\left(\left(I_S^f\right)^2+2I_S^fI_S^b+2I_P^fI_S^f+2I_P^bI_S^f\right)+ $$
$$+gI_S^f\cdot\left(I_P^f+I_P^b\right)-\sigma_SQI_S^f \qquad (22)$$

$$\left(-\frac{\partial}{\partial z}+\frac{1}{c}\frac{\partial}{\partial t}\right)I_S^b(t,z)=-\beta\cdot\left(\left(I_S^b\right)^2+2I_S^fI_S^b+2I_P^fI_S^b+2I_P^bI_S^b\right)+ $$
$$+gI_S^b\cdot\left(I_P^f+I_P^b\right)-\sigma_SQI_S^b \qquad (23)$$

$$Q(t,z)'_t=-\frac{1}{t_{FC}}Q+\beta\cdot\left(\frac{\left(I_P^f\right)^2+\left(I_P^b\right)^2+4I_P^fI_P^b}{2hv_P}+\frac{\left(I_S^f\right)^2+\left(I_S^b\right)^2+4I_S^bI_S^f}{2hv_S}+\right.$$
$$\left.+\frac{4I_P^fI_S^f+4I_P^fI_S^b+4I_P^bI_S^f+4I_P^bI_S^b}{h\cdot\left(v_P+v_S\right)}\right). \qquad (24)$$

where $I_P^f(t,z)$ and $I_P^b(t,z)$ are intensities of forward and backward pump waves, $I_S^f(t,z)$ and $I_S^b(t,z)$ are intensities of forward and backward Stokes waves. A steady-state regime was supposed for equation set (20)-(24).

Assuming that pump pulse duration is sufficiently higher than the round-trip time of the cavity we averaged equations (20)-(24) and obtained the following equation set:

$$\frac{\partial}{\partial z} I^f{}_P(t,z) = -\beta \cdot I_P{}^f \cdot \left(I_P{}^f + 2\left(I_P{}^b + I_S \right) \right) - \frac{\nu_P}{\nu_S} g I_P{}^f I_S - \sigma_P Q I_P{}^f, \tag{25}$$

$$-\frac{\partial}{\partial z} I^b{}_P(t,z) = -\beta \cdot I_P{}^b \cdot \left(I_P{}^b + 2\left(I_P{}^f + I_S \right) \right) - \frac{\nu_P}{\nu_S} g I_P{}^b I_S - \sigma_P Q I_P{}^b, \tag{26}$$

$$\frac{L_C}{c} \frac{\partial}{\partial t} I_S(t,z) = -\beta L_{CR} I_S \cdot \left(\frac{3}{2} I_S + 2 I_P \right) + g L_{CR} I_S I_P - \sigma_S L_{CR} Q I_S - L_S I_S, \tag{27}$$

$$Q(t,z)'_t = -\frac{1}{t_{FC}} Q + \beta \cdot \left(\frac{\frac{1}{L_{CR}} \int\limits_0^{L_{CR}} \left(\left(I_P{}^f \right)^2 + \left(I_P{}^b \right)^2 + 4 I_P{}^f I_P{}^b \right) dz}{2 h \nu_P} + \frac{3}{2} \frac{I_S{}^2}{2 h \nu_S} + \frac{4 I_P I_S}{h \cdot \left(\nu_P + \nu_S \right)} \right), \tag{28}$$

where

$$I_P = \frac{1}{L_{CR}} \int\limits_0^{L_{CR}} \left(I_P{}^f + I_P{}^b \right) dz, \tag{29}$$

$$I_S = \frac{1}{L_{CR}} \int\limits_0^{L_{CR}} \left(I_S{}^f + I_S{}^b \right) dz, \tag{30}$$

$$L_S = -\ln\left(\sqrt{R_{S1} R_{S2}} \right), \tag{31}$$

where R_{S1} and R_{S2} – relativities of input and output mirrors at Stokes wavelength.

Raman laser threshold

As in the case of single-pass SRS for estimation of Raman threshold the depletion of pump radiation due to Raman conversion can be neglected and equations (25)-(28) can be simplified as follows:

$$\frac{\partial}{\partial z} I^f{}_P(t,z) = -\beta \cdot I_P{}^f \cdot \left(I_P{}^f + 2 I_P{}^b \right) - \sigma_P Q I_P{}^f, \tag{32}$$

$$-\frac{\partial}{\partial z} I^b{}_P(t,z) = -\beta \cdot I_P{}^b \cdot \left(I_P{}^b + 2 I_P{}^f \right) - \sigma_P Q I_P{}^b, \tag{33}$$

$$\frac{L_C}{c} \frac{\partial}{\partial t} I_S(t,z) = (g - 2\beta) \cdot L_{CR} I_S I_P - \sigma_S L_{CR} Q I_S - L_S I_S, \tag{34}$$

$$Q(t,z)'_t = -\frac{1}{t_{FC}} Q + \frac{\beta}{2 h \nu_P} \frac{1}{L_{CR}} \int\limits_0^{L_{CR}} \left(\left(I_P{}^f \right)^2 + \left(I_P{}^b \right)^2 + 4 I_P{}^f I_P{}^b \right) dz. \tag{35}$$

The solution of equation (34) is the following:

$$I_S\left(t,z\right)=I_{S0}\exp\left(\frac{c}{L_C}\int_0^t\left(\left(g-2\beta\right)\cdot L_{CR}I_P-\sigma_S L_{CR}Q-L_S\right)dt\right),\qquad(36)$$

Similarly to (14) the Raman threshold occurs when the exponent in (36) is equal to 25:

$$G_R\left(t\right)=\frac{c}{L_C}\int_0^t\left(\left(g-2\beta\right)\cdot L_{CR}I_P-\sigma_S L_{CR}Q-L_S\right)dt'\approx25,\qquad(37)$$

So, equations (32),(33),(35), and (37) were used to determine the threshold for a silicon based Raman laser. Calculations were made for pump pulses with durations of 50 ns and 100 ns, respectively.

Results of threshold calculations are presented in Figure II.1.3.1. This figure shows the dependencies of output coupler reflectivities at Stokes wavelength required to get Raman threshold at a given conditions on the pump energy density. The cases of output coupler reflectivity at pump wavelength equal to 0% and to 100% were considered. Figure II.1.3.1 shows that the use of output coupler with high reflectivity at pump wavelength leads at certain conditions to the increase of threshold energy density. For instance, for pump pulse duration of 100 ns (Figure II.1.3.1b), the value of Raman gain equal to 20 cm/GW, and output coupler reflectivity at Stokes wavelength of 60 % the threshold energy density for lasing increases from 1.6 J/cm^2 to 3.5 J/cm^2, when the output coupler reflectivity at pump wavelength increases from 0% to 100%. This is in contrast to conventional Raman lasers, where the use of two pump passes through the cavity always decreases Raman threshold. In silicon the pump beam, reflected by the output coupler, increases pump intensity in the cavity. This results not only in a higher Raman gain, but in higher losses due to FCA and TPA too. Taken into account that FCA losses depend more on pump intensity than Raman gain, the pump intensity increase can lead to an increase of Raman threshold. Figure II.1.3.1 shows that such behavior occurs in region where output coupler reflectivity at Stokes wavelength is low and threshold energy density is high. For instance for a Raman gain coefficient of 10 cm/GW the Raman threshold can be reached only for one pass of the pump beam through the cavity. In cases, where the threshold energy is low, Raman gain is mainly dominated on FCA and two passes of pump lead to a lowering of the Raman threshold, as known from conventional lasers.
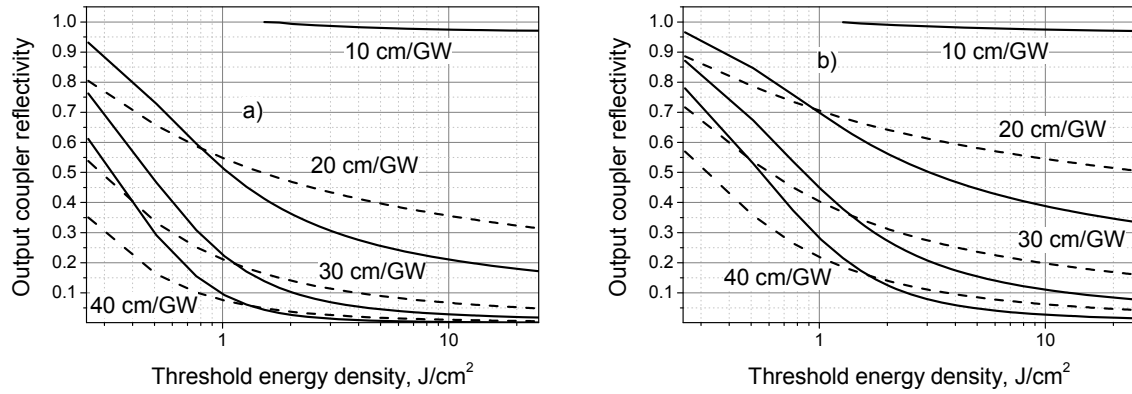
Figure II.1.3.1: Output coupler reflectivities at Stokes wavelength required to reach the Raman threshold at a given pump energy density. Calculations were made for pump pulse duration (a) of 50 ns and (b) of 100 ns, for different values of Raman gain coefficients, and for output coupler reflectivity at pump wavelength of 0% (solid lines) and of 100 % (dashed lines).

So, Figure II.1.3.1 shows that the oscillation of the silicon Raman laser is possible in case of long pump pulses (50 and 100 ns) for all considered values of Raman gain coefficients.

Raman laser conversion efficiency

In a Raman laser not only the pump beam diameter should be optimized to provide the highest output energy, but also the output coupler reflectivity at the Stokes wavelength. Figure II.1.3.2 shows the results of such optimization performed for a Raman laser with crystal length of 3 cm and pump pulse durations of 50 ns and 100 ns. A cavity length was assumed also to be 3 cm. Figure II.1.3.2 presents the dependencies of the output Stokes energy at the pump energy of 20 mJ on the output coupler reflectivity for the optimal values of the pump beam diameter. It can be seen, that the exploitation of the output coupler with 100% reflectivity at the pump wavelength provides higher Stokes energy than that for the output coupler reflectivity of 0%. For the Raman gain coefficient of 40 cm/GW output energies of 1.4 mJ (efficiency is 7%) and 1 mJ (efficiency is 5%) can be reached for pump pulses of 50 ns and 100 ns, respectively. This efficiency can be increased by the increase of crystal length. For instance, a 10 cm long Si-crystal provides a conversion efficiency of about 10% (Figure II.1.3.2a, dotted line).
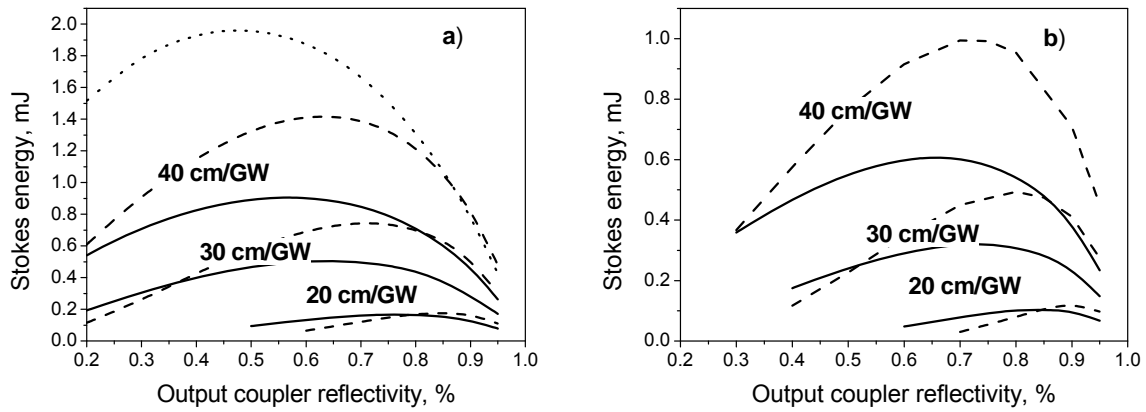
19

Figure II.1.3.2: Dependence of Stokes energy on output coupler reflectivity at the Stokes wavelength. The calculations were made for pump pulse duration (a) of 50 ns and (b) of 100 ns, for different values of Raman gain coefficient, and for the output coupler reflectivity at pump wavelength of 0% (solid lines) and of 100 % (dashed lines). The dotted line shows the results for a 10 cm long crystal.

So, the numerical calculations in bulk silicon show that the Raman conversion in bulk silicon is possible even at room temperature. For conversion of short pulses (hundreds of picoseconds - nanoseconds) a single-pass or multi-pass generation scheme can be used. The conversion efficiency of up to 25% can be reached for pumping with pulses of 200 ps duration. For conversion of pump pulses with duration of several tens or hundreds of nanoseconds a Raman laser can be exploited. For pump pulse duration of 50 ns conversion efficiency can be up to 10%.

II.1.4 Calculation of Raman conversion in Bulk-Si Raman laser at low temperature

The theoretical model developed in the frame of the SiliconLight project and presented in the previous sections of this chapter was also used for description of Raman laser operation at low temperature (10 K). The exploitation of low temperatures decreases bandwidth of absorption lines due to electron transitions [1]. This allows the use of pump radiation with frequency close to the electron transition frequency. Under these resonant conditions Raman nonlinearity increases strongly. For instance, radiation with wavelength of 1064 nm can be used for pumping of a low temperature silicon Raman laser. At room-temperature this radiation is absorbed by silicon very strongly and can not be used. In addition, the decrease of temperature leads to the decrease of Raman line bandwidth. The Raman gain coefficient is inversely proportional to the value

20

of this bandwidth [14]. Thus, both the use of pump wavelength close to a resonant transition and the decrease of Raman line bandwidth result in an extreme increase of the Raman gain coefficient. At wavelength of 1064 nm the value of the Raman gain coefficient is 190 cm/GW [1], which is 19 times higher than the value for barium nitrate (10 cm/GW [15]), a well-known Raman crystal. Also the decrease of temperature results in a decrease of the free-carriers absorption cross-section.

Operation of a low-temperature Raman laser was demonstrated for the first time by our project partner TUB. Our task was to describe theoretically this operation. Equations (25)-(28) have been used for this purpose. The following values for the model parameters were used: temperature is 10 K, β = 10 cm/GW [1], g = 190 cm/GW [1], t_C = 1 µs [8], L_{CR} = 3 cm. Values for cross-section area of free-carriers are not known at temperature of 10K. The cross-section area at pump wavelength was a fitting parameter. The cross-section area at Stokes wavelength was calculated as follows [5]:

$$\sigma_S = \sigma_P \cdot \left(\frac{\lambda_S}{\lambda_P} \right)^2 , \tag{38}$$

where the pump wavelength (λ_P) is 1064 nm, while the Stokes wavelength is 1127 nm (λ_S).

It was necessary to take a free-carrier lens formation into account. Indeed, two-photon absorption induces free-carrier formation. This leads not only to free-carrier losses, but to a change of refractive index of silicon [4]. A spatially nonuniform pump beam creates a nonuniform change of refractive index. This means formation of a lens. This lens was calculated using the following expression:

$$\Delta n = n_{eh} \int Q(z) dz , \tag{39}$$

where the parameter n_{eh} is for silicon equal to $-9 \cdot 10^{-22}$ cm^2[4], Q is the solution of equations (25)-(28).

The spatial distribution of change of refractive index calculated for a Gaussian pump beam with diameter of 1 mm is presented in Figure II.1.4.1. It can be seen that the refractive index distribution is almost the same as for the spatial distribution of the pump beam.
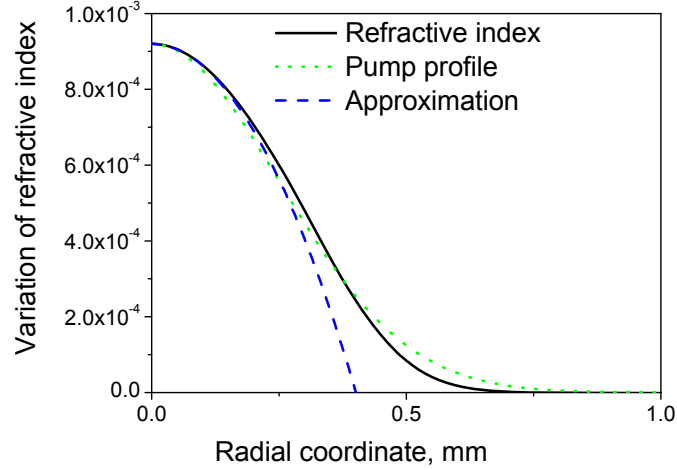
Figure II.1.4.1: Distribution of the absolute value of variation of refractive index by induced free-carries along the radial coordinate.

In order to calculate the effect of this free-carrier lens, the calculated distribution of refractive index was approximated with a parabolic function [16]:

$$n(r) = n_0 \cdot \left(1 - \gamma r^2\right), \tag{40}$$

where n_0 is the refractive index in the center of the crystal, γ is a fitting parameter, which determines the refractive power of induced lens (D):

$$D = 2\gamma n_0 L_{CR}. \tag{41}$$

The induced lens acts as a thick lens with the following ABCD-matrix [16]:

$$\begin{pmatrix} A & B \\ C & D \end{pmatrix} = \begin{pmatrix} \cos\left(\sqrt{2\gamma}z\right) & \dfrac{1}{\sqrt{2\gamma}n_0}\sin\left(\sqrt{2\gamma}z\right) \\ -\sqrt{2\gamma}n_0\sin\left(\sqrt{2\gamma}z\right) & \cos\left(\sqrt{2\gamma}z\right) \end{pmatrix}, \tag{42}$$

Using matrix (42) and the ABCD-method [16] for calculation of the Gaussian beam evolution, the increase of pump beam diameter during propagation along the crystal was determined. The dependence of pump beam diameter on the longitudinal coordinate z is shown in Figure II.1.4.2. As can be seen, the Rayleigh range (distance which corresponds to a $\sqrt{2}$ times increase of pump beam diameter) is equal to 0.85 cm. This range is sufficiently shorter than the crystal length (3 cm) and the value of this range should be used in equations (25)-(28) instead of the crystal length.
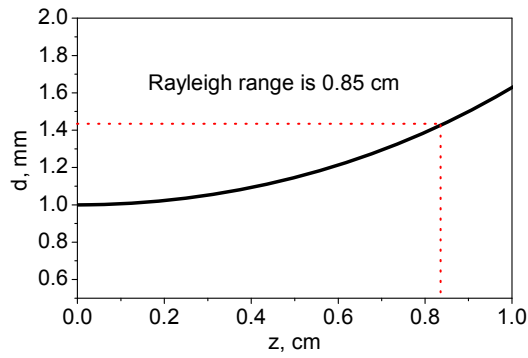
Figure II.1.4.2: Dependence of pump beam diameter on the longitudinal coordinate in silicon crystals.
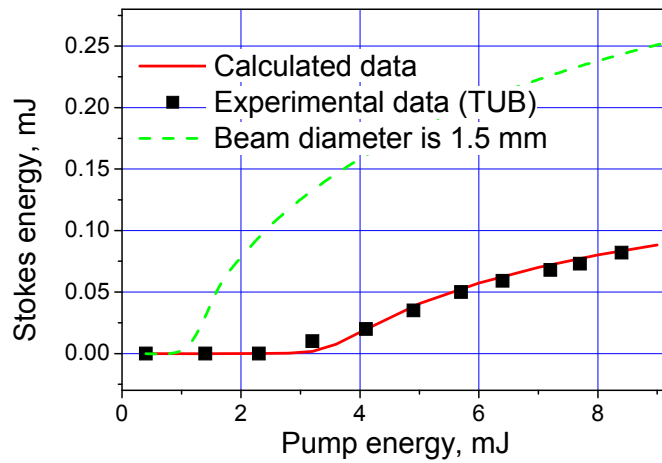

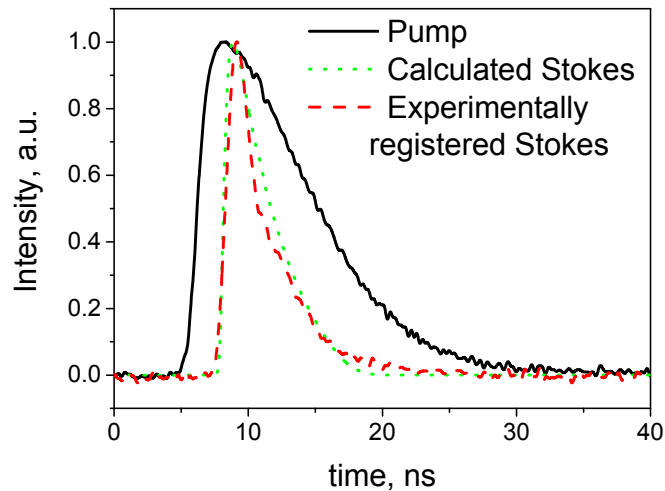Figure II.1.4.3: Dependencies of Stokes energy on pump pulse energy.

Figure II.1.4.4: Experimental oscilloscope traces of pump and Stokes pulses obtained in TUB and calculated Stokes pulse shape.

Calculation results are presented in Figure II.1.4.3 and II.1.4.4 together with experimental results obtained by the project partner TUB. Figure II.1.4.3 demonstrates the dependence of output Stokes energy on pump pulse energy, Figure II.1.4.4 presents oscilloscope traces of pump and Stokes beam. The pump oscilloscope trace presented in Figure II.1.4.4 was used in our calculation as pump pulse shape. In both figures a good quantitative correspondence is seen. This means that the developed theory can well describe Raman generation in silicon crystals. In addition, this theory can predict ways for optimization of Raman lasers. For instance, our calculations show that an increase of pump beam diameter up to 1.5 mm leads to an 2.5 times increase of the output Stokes energy. The calculated dependence of Stokes energy on pump energy for beam diameter of 1.5 mm is also presented in Figure II.1.4.3.

II.2 Theoretical investigation of stimulated Raman scattering in SOI-waveguide

SOI-waveguides for Raman lasers and modulators were designed and investigated during the project. The first part of this chapter contains results of design of SOI-waveguides, the calculation of coupling between SOI-based Raman laser and input SOI-waveguide. The second part is devoted to the numerical investigation of Raman threshold for designed SOI-waveguides, the optimization of their parameters. Results of numerical simulations and design of electric contacts for electro-optical modulators are presented in the third part.

II.2.1 Modeling of coupling between SOI-based Raman cavity and input SOI-waveguide

One important task in design of a Raman laser cavity is the design of a coupler region between an input waveguide and the waveguide of the Raman cavity (see Figure II.2.1.1). This coupler should provide coupling of pump radiation into the waveguide "racetrack" of the Raman laser. Raman generation occurs within the "racetrack", the long, oval form waveguide, and results in conversion of pump radiation to the first Stokes radiation. The generated Stokes radiation should be coupled out from the Raman cavity to an output waveguide. In Figure II.2.1.1 a case illustrated where the same waveguide acts both as input and output.
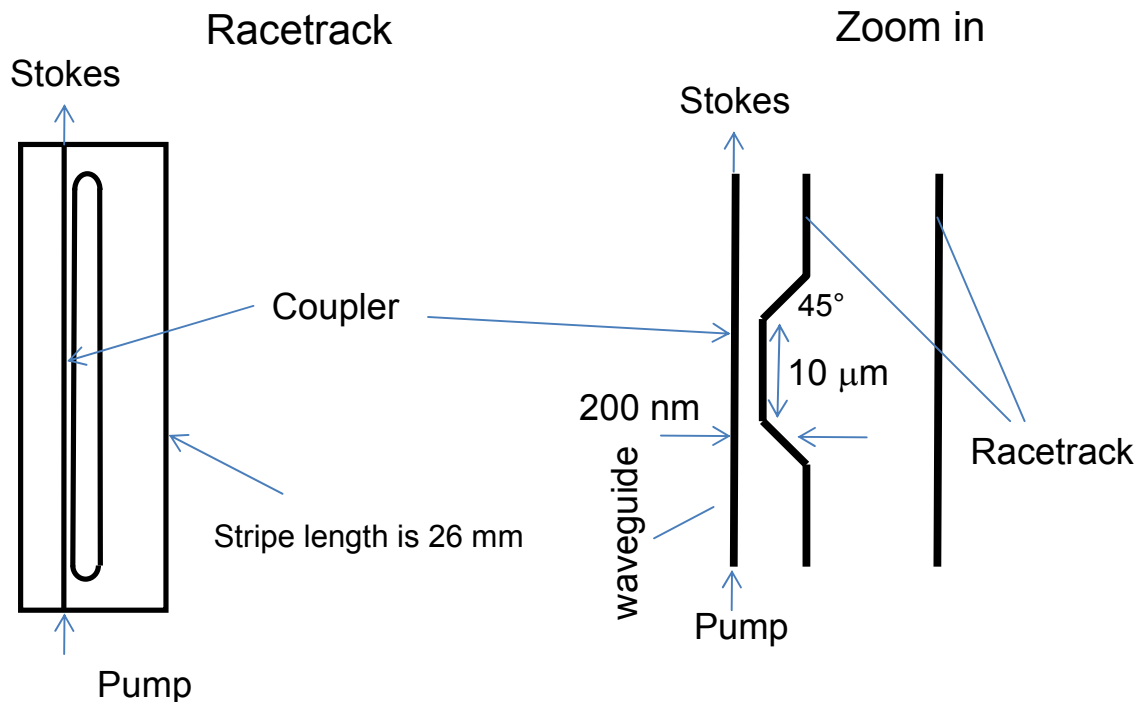
Figure II.2.1.1: Sketch demonstrating the base concept of frequency conversion in a SOI waveguide. The pump wave propagates within the input channel waveguide, and is coupled into the racetrack where conversion into the Stokes wave occurs. Subsequently, the converted wave couples back into the main waveguide.

The wavelengths of pump and Stokes radiations are different. The task was to find parameters for a coupler, which provides certain coupling ratios at these two wavelengths simultaneously. These coupling ratios for both pump and Stokes radiation should be optimized. Optimal coupling at pump wavelength should provide a highest value of intracavity power and, hence, higher values of single-pass Raman gain. An optimal coupling ratio at Stokes wavelength should provide appropriate values of threshold power and of generation efficiency (Optimization of values for these coupling ratios is presented in the next chapter "*II.2.2 Numerical investigation of Raman threshold in SOI-based Raman ring laser*").

Calculation of coupler parameters was performed numerically for a pump wave wavelength of 1341.4 nm and a first Stokes wave wavelength of 1442.1 nm. The process of light coupling between two waveguides depends on many parameters. The first one is the effective refractive index. As seen from Figure II.2.1.2 the intensity of the light propagating through the waveguide is mostly concentrated within the core. Only a small part of electrical field (so-called evanescence wave) penetrates into the surrounding. Exactly this small part is responsible for the energy exchange between two

close-by waveguides. Thus, the efficiency of conversion is better when the distance between waveguides is smaller than the wavelength of the propagating light.
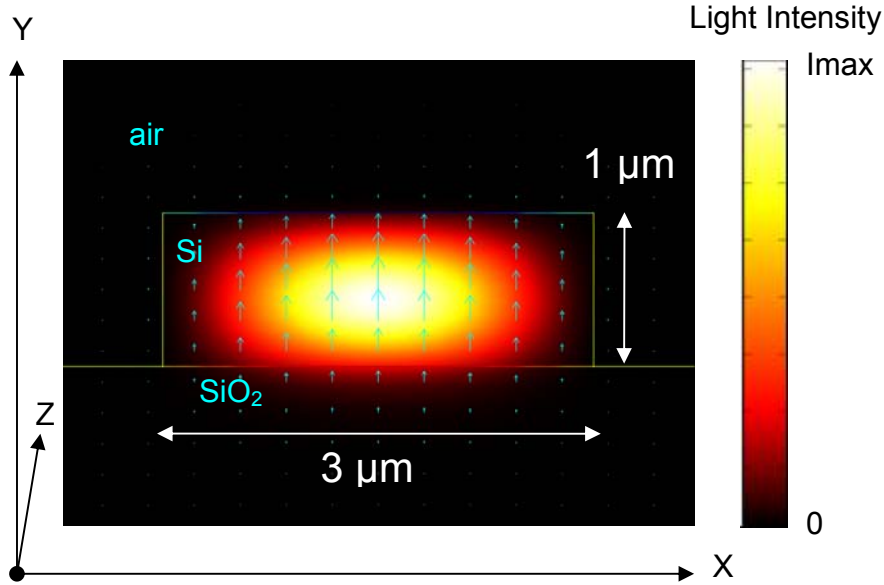

Figure II.2.1.2: Field distribution in a cross-section of a SOI waveguide. Maximum of intensity is concentrated in the center of the waveguide.

Before construction of the coupling element, an analysis of the optical field distribution within waveguide was performed. The mode analysis is made on a cross-section in the *xy*-plane of the waveguide. The wave propagates in the *z*- direction and has the form[17]:

$$\mathbf{H}(x, y, z, t) = \mathbf{H}(x, y)e^{j(\omega t - \beta z)} \tag{43}$$

where ω is the angular frequency and β is the propagation constant. An eigenvalue equation for the magnetic field H is derived from Helmholtz equation[18]:

$$\nabla \times \left(n^{-2} \nabla \times \mathbf{H} \right) - k_0^2 \mathbf{H} = 0 \tag{44}$$

where *n* is the refractive index which is solved for the eigenvalue *λ* = −*jβ*. The wave number of free space k_0 is defined as:

$$k_0 = \omega\sqrt{\varepsilon_0 \mu_0} = \frac{\omega}{c_0} \tag{45}$$

where c_0 is the speed of light in vacuum.

When studying the characteristics of optical waveguides, the effective mode index of a confined mode is depicted as:

$$n_{eff} = \frac{\beta}{k_0}.$$

(46)

The effective refractive index of a certain waveguide mode (typically TE_0 or TM_0) is used for further calculations of wave propagation in SOI waveguides.

Applying the effective refractive index instead of bulk (pure material) refractive index allows to use a 2D model instead of a 3D model. For finite element analysis, two dimensional modeling requires much less computational resources (memory and CPU time) than a 3D modeling.

Light propagation within a waveguide is the power flow through the cross-section of the waveguide.

For time-harmonic (sinusoidal) electromagnetic fields, the average power flow over time is often more useful, and can be found as follows,

$$
\begin{aligned}
\mathbf{S} = \mathbf{E} \times \mathbf{H} &= \mathrm{Re}\left(\mathbf{E}e^{j\omega t}\right) \times \mathrm{Re}\left(\mathbf{H}e^{j\omega t}\right) = \frac{1}{2}\left(\mathbf{E}e^{j\omega t} + \mathbf{E}^* e^{-j\omega t}\right) \times \frac{1}{2}\left(\mathbf{B}e^{j\omega t} + \mathbf{H}^* e^{-j\omega t}\right) = \\
&= \frac{1}{4}\left(\mathbf{E} \times \mathbf{H}^* + \mathbf{E}^* \times \mathbf{H} + \mathbf{E} \times \mathbf{H}e^{2j\omega t} + \mathbf{E}^* \times \mathbf{H}^* e^{-2j\omega t}\right) = \\
&= \frac{1}{4}\left(\mathbf{E} \times \mathbf{H}^* + \left(\mathbf{E} \times \mathbf{H}\right)^* + \mathbf{E} \times \mathbf{H}e^{2j\omega t} + \left(\mathbf{E} \times \mathbf{H}^* e^{-2j\omega t}\right)^*\right) = \\
&= \frac{1}{2}\mathrm{Re}\left(\mathbf{E} \times \mathbf{H}^*\right) + \frac{1}{2}\mathrm{Re}\left(\mathbf{E} \times \mathbf{H}e^{2j\omega t}\right)
\end{aligned}
$$

(47)

The average over time is given as

$$\overline{\mathbf{S}} = \frac{1}{T}\int_0^T S(t)dt = \frac{1}{T}\int_0^T \frac{1}{2}\mathrm{Re}\left(\mathbf{E} \times \mathbf{H}^*\right) + \frac{1}{2}\mathrm{Re}\left(\mathbf{E} \times \mathbf{H}e^{2j\omega t}\right)dt$$

(48)

The second term is a cosinusoidal curve $\mathrm{Re}\left(e^{2j\omega t}\right) = \cos 2\omega t$ whose average will be zero. Finally, the power flow is given by the time-averaged Poynting vector S_{av} [19],

$$\mathbf{S}_{av} = \frac{1}{2}\mathrm{Re}\left(\mathbf{E} \times \mathbf{H}^*\right)$$

(49)

The amount of power flowing out of a waveguide element is given by the normal component of the Poynting vector,

$$\mathbf{n} \times \mathbf{S}_{\mathbf{av}} = \mathbf{n} \cdot \frac{1}{2} \operatorname{Re}\left(\mathbf{E} \times \mathbf{H}^*\right) \qquad (50)$$

where $\mathbf{n}$ is a unit normal vector to the end face of waveguide.

In the following the power flow is expressed directly in terms of the electric field for TE, TM, and TEM waves.

For TE mode the impedance Z_{TE} can be written as:

$$Z_{TE} = \frac{\omega\mu}{\beta} \qquad (51)$$

For TM mode the impedance Z_{TM} is:

$$Z_{TM} = \frac{\beta}{\omega\varepsilon}, \qquad (52)$$

where ω is the angular frequency of the wave, μ is the permeability, and β is the propagation constant. The power flow then becomes:

$$\mathbf{n} \times \mathbf{S}_{\mathbf{av}} = \frac{1}{2}\mathbf{n} \cdot \operatorname{Re}\left(\mathbf{E} \times \mathbf{H}^*\right) = -\frac{1}{2}\operatorname{Re}\left(\mathbf{E} \cdot \left(\mathbf{n} \times \mathbf{H}^*\right)\right) = \frac{1}{2Z_{TE}}|\mathbf{E}|^2 \qquad (53)$$

After definition of the boundary conditions and the following simulation one can obtain the distribution of light power (intensity) within the waveguide. Varying the geometrical structure, material parameters, and wavelength different propagation images are observed. The task was to get a configuration where as much as possible of pumping light is coupled to the racetrack.

28

As a result an optimal configuration was found which couples-in the pumping wave completely into the racetrack and after one round trip couples it completely back to the waveguide (Figure II.2.1.3).
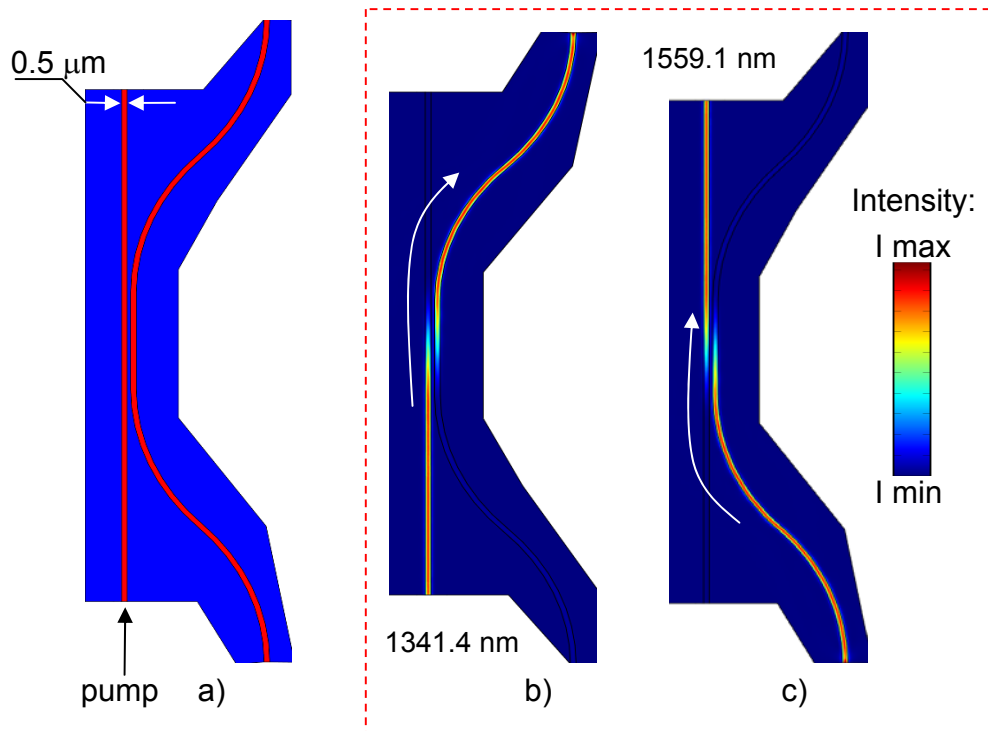

Figure II.2.1.3: Scheme of waveguide-racetrack coupler (a) and light coupling into (b) and from (c) racetrack. In Figures (b) and (c) the color map describes the intensity distribution within the waveguide.

The racetrack is 20-25 mm long, i.e. has an interaction length of ~5 cm. Having a high efficiency of conversion into the Stokes wavelength the light will be converted during a single trip over the racetrack.

Waveguide structures designed according to the methods described above were implemented in a SOI-based chip. Figure II.2.1.4 shows a micro-photograph of a separate waveguide. An atomic-force-microscope (AFM) image of this waveguide is show in Figure II.2.1.5.
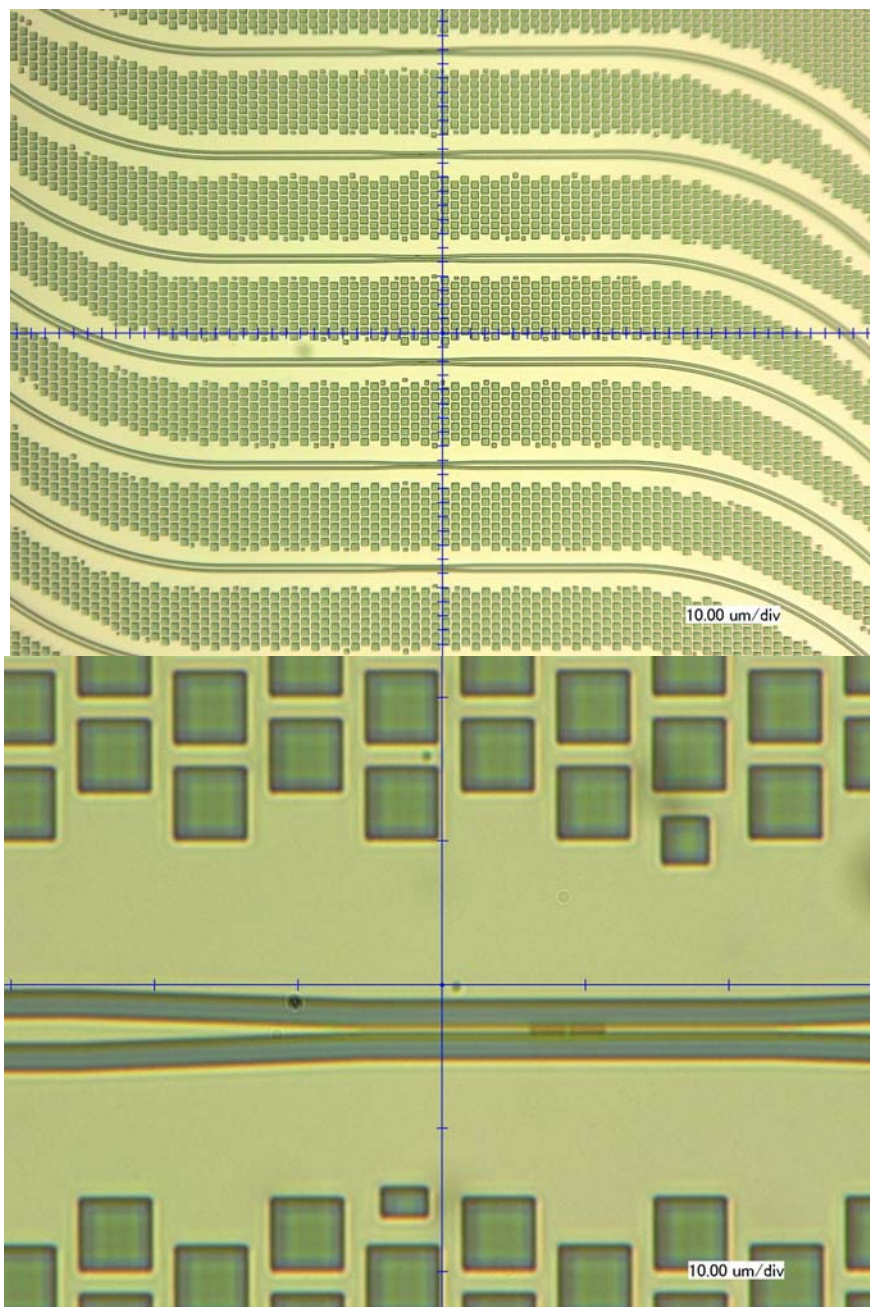
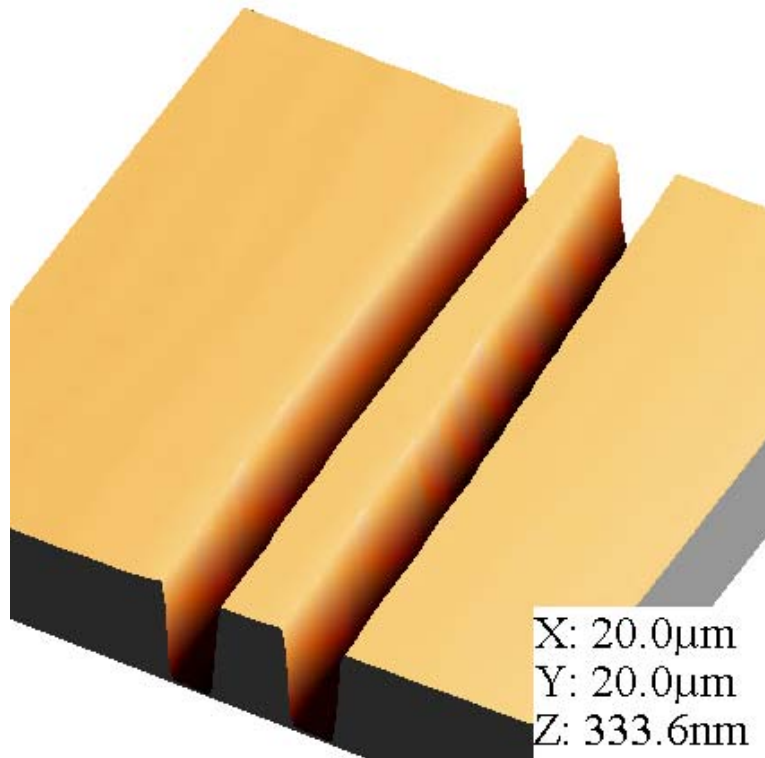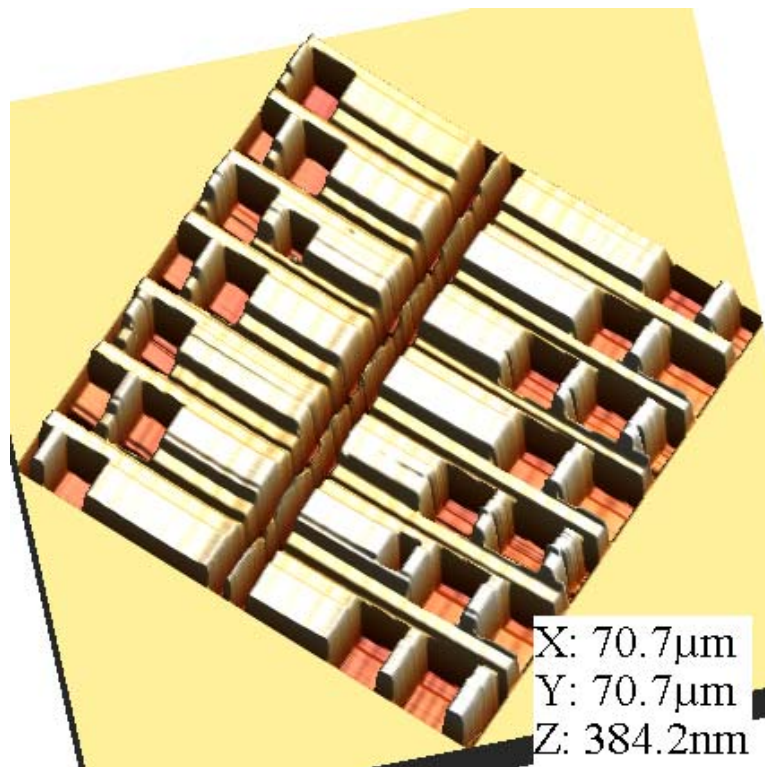Figure II.2.1.4: Microphotograph of a waveguide-containing chip.

X: 70.7μm
Y: 70.7μm
Z: 384.2nm

X: 20.0μm
Y: 20.0μm
Z: 333.6nm

Figure II.2.1.5: AFM-images of a waveguide. X, Y, and Z – amplitudes of the AFM-scan.

II.2.2 Numerical investigation of Raman threshold in a SOI-based Raman ring laser

This section considers stimulated Raman scattering in a ring structure presented in Figure II.2.1.1. The main goal was to determine parameters of these structures, which make the Raman conversion possible. These parameters are cavity length (or length of racetrack), and coupling ratios of the coupler at pump and Stokes wavelengths. These are the parameters, which can be controlled with proper design of the structure, as it was described in the previous section.

The following equations were used for description of stimulated Raman scattering in ring lasers [5, 7]:

$$\frac{dI_P(z,t)}{dz} = \left(\alpha_P - \beta I_P - \frac{\sigma_P \beta t_C}{2 \cdot h\nu_P} I_P^2 \right) I_P \, , \tag{54}$$

$$\frac{dI_S(z,t)}{dz} = \left(gI_P - \alpha_S - 2\beta I_P - \frac{\sigma_S \beta t_C}{2 \cdot h\nu_P} I_P^2 \right) I_S \, , \tag{55}$$

where α_P and α_S are propagation losses at pump and Stokes wavelengths, respectively. It should be noted that equations (54) and (55) differ from equations (10)-(12), because for a SOI-waveguide free-carrier lifetime is small [20] and equation (12) can be eliminated. Equations (54) and (55) do not consider pump depletion due to Raman conversion. This means that an operation of the Raman laser near threshold was assumed. This assumption is correct for Raman threshold determination.

After averaging equations (54), (55) we can obtain the following equations for pump and Stokes powers:

$$\frac{dP_P(z,t)}{dz} = \left(-\beta \frac{P_P}{S_3} - \frac{\sigma_P \beta t_C}{2 \cdot h\nu_P} \frac{P_P^2}{S_4^2} - \alpha_P \right) P_P \, , \tag{56}$$

$$\frac{dP_S(z,t)}{dz} = \left((g_P - 2\beta) \frac{P_P}{S_1} - \frac{\sigma_S \beta t_C}{2 \cdot h\nu_P} \frac{P_P^2}{S_2^2} - \alpha_S \right) P_S \, , \tag{57}$$

where S_i are efficient areas, which can be determined as follows:

$$S_1 = \frac{\iint I_S(S)dS \iint I_P(S)dS}{\iint I_S(S)I_P(S)dS} \tag{58}$$

$$S_2 = \sqrt{\frac{\iint I_S(S)dS\left(\iint I_P(S)dS\right)^2}{\iint I_S(S)I_P^{\,2}(S)dS}}$$ (59)

$$S_3 = \frac{\left(\iint I_P(S)dS\right)^2}{\iint I_P^{\,2}(S)dS}$$ (60)

$$S_4 = \sqrt{\frac{\left(\iint I_P(S)dS\right)^3}{\iint I_P^{\,3}(S)dS}}\,,$$ (61)

where $I_P(S)$ and $I_S(S)$ are the distribution of pump and Stokes beams in the cross-section of the waveguide, respectively.

Equations (56) and (57) describe the change of pump and Stokes powers while propagating along the cavity. The generation threshold is reached when the gain G_S of Stokes power during one pass through the cavity is equal or higher than the losses L_S in the coupling region:

$$G_S \geq L_S,$$ (62)

where gain G_S and losses at coupling L_S are calculated according to:

$$G_S = \int\limits_{L_{CAV}} \left((g_P - 2\beta)\frac{P_P(z)}{S_1} - \frac{\sigma_S \beta t_C}{2 \cdot h\nu_P}\frac{P_P^{\,2}(z)}{S_2^{\,2}} - \alpha_S \right) dz,$$ (63)

$$L_S = -\ln\left(\sqrt{R_S}\right),$$ (64)

where R_S is the reflectivity of the output coupling mirror.

Numerical calculations were performed for a pump wavelength of 1432 nm. The corresponding first Stokes wavelength is 1547 nm. Values of other parameters were the following β = 0.5 cm/GW [7], σ_P = 1.24×10^{-17} cm^2, σ_S = 1.45×10^{-17} cm^2 [5]. The value of the Raman gain coefficient was varied from 10 to 40 cm/GW [4, 6, 7, 9-12]. Calculations were made for SOI-waveguide with a cross-section of 220 nm x 445 nm. The field distribution of pump and Stokes radiation was calculated for this waveguide. This distribution was practically the same for these radiations and is presented in Figure II.2.2.1. Using this distribution the following efficient areas S_i were calculated (see equations (58)-(61)): $S_1 \approx S_2$=8.3·10^{-10} cm^2, $S_3 \approx S_4$=7.3·10^{-10} cm^2. Free-carrier life-time

depends on the waveguide cross-section and was assumed to be in the range of 0.3-1 ns [20]. Propagation losses were varied between 5-10 dB/cm.
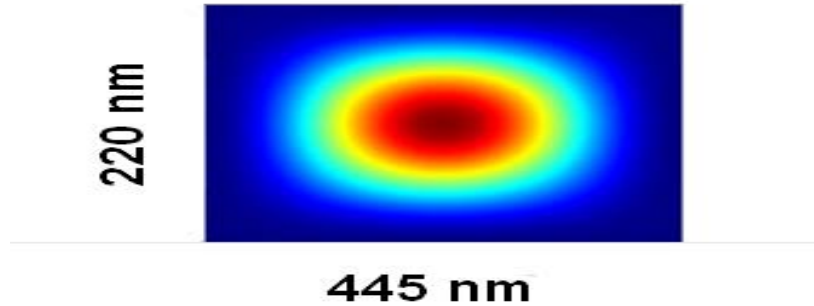

Figure II.2.2.1: Calculated field distribution in a 220 nm x 445 nm SOI waveguide.
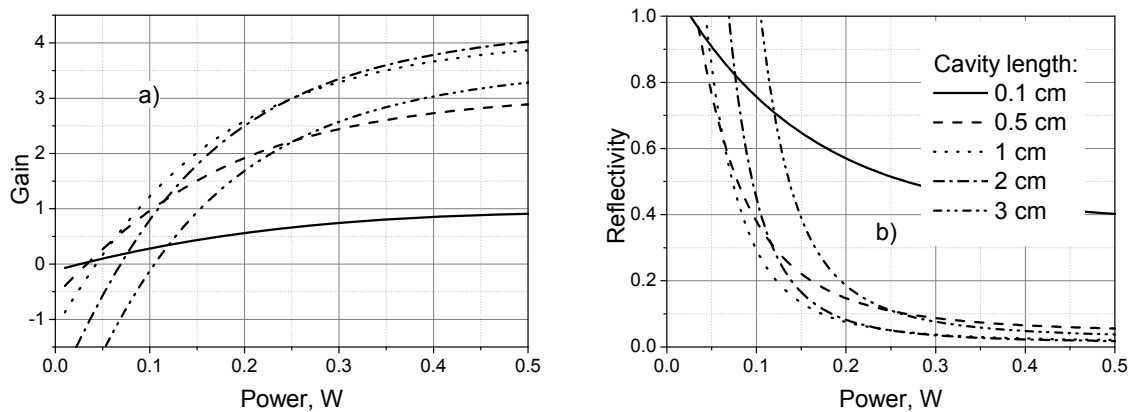

Figure II.2.2.2: Dependencies of single-pass gain (a) and of reflectivity (b) of the coupling at Stokes wavelength, which is required to get the Raman threshold, on pump power inside the cavity of the Raman ring laser. The dependencies were calculated for different lengths of cavity and for the following parameters of cavity: g = 40 cm/GW, α = 5 dB/cm, t_{FC} = 1ns.

Results of numerical calculation of the Raman threshold performed for g = 40 cm/GW, α = 5 dB/cm, t_{FC} = 1ns are presented in Figure II.2.2.2. Figure II.2.2.2a shows the dependencies of single-pass gain (G_S) on pump power in the cavity calculated for different values of cavity length. A negative value of single-pass gain means that propagation losses are higher than the Raman gain and Raman generation can not be obtained even for coupling with a very high reflectivity. If single-pass gain is positive, the Raman generation is possible for a coupling with a reflectivity higher than a certain value. The dependencies of this reflectivity on pump power are presented in Figure II.2.2.2b. This figure shows that lowest possible threshold power (25 mW) can be obtained for a cavity length of 0.1 cm. However, this requires a value of coupling reflectivity close to 100%. For coupling reflectivity of 50%, threshold power increases up

to 300 mW. The values of cavity length equal to 0.5 cm or 1 cm provide a little bit higher minimum value of threshold power, but are more stable against the decrease of coupling reflectivity. For instance, for coupling reflectivity of 50% the threshold power is less than 80 mW. So, a cavity length of 0.5-1 cm is optimal for the considered case.
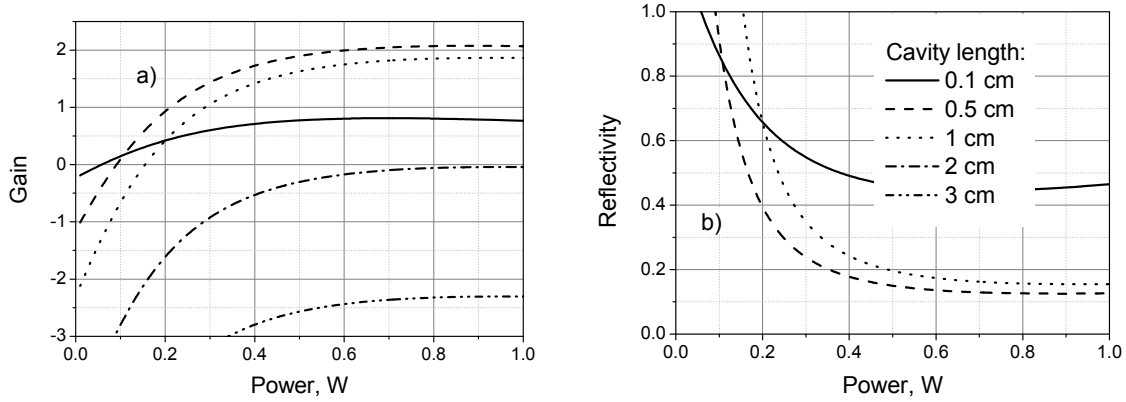

Figure II.2.2.3: Dependencies of single-pass gain (a) and of reflectivity (b) of the coupling at Stokes wavelength, which is required to get Raman threshold, on pump power inside the cavity of the Raman ring laser. The dependencies were calculated for different lengths of cavity and the following parameters of cavity: g = 40 cm/GW, α = 10 dB/cm, t_{FC} = 1 ns.

Figure II.2.2.4 shows the calculation results obtained for the optimal case: Raman gain coefficient equal to 80 cm/GW and free-carriers life-time of 0.3 ns. Again, optimal values of cavity length are 0.1, 0.5, and 1 cm. It should be noted that the sensitivity of threshold power for a 0.1 cm long cavity on coupling reflectivity in this case is acceptable both for propagation losses of 5 dB/cm and 10 dB/cm. Figure II.2.2.5 presents the calculation results obtained in the worst case: Raman gain coefficient equal to 20 cm/GW. Figure II.2.2.5a corresponds to α = 5 dB/cm and t_{FC} = 1ns, while Figure II.2.2.5b was plotted for α = 10 dB/cm and t_{FC} = 0.5 ns. Further deterioration of cavity parameters makes Raman generation impossible. It can be seen that for the case presented in Figure II.2.2.5a the optimal cavity lengths are 0.5 and 1 cm. Generation in a 0.1 cm long cavity is possible only for a high values of coupling reflectivity. For the case shown in Figure II.2.2.5b the cavity length should be 0.1-0.5 cm.

An increase of propagation losses evidently leads to an increase of threshold power. Figure II.2.2.3 shows calculations results obtained for α = 10 dB/cm. It can be seen that Raman generation is available only for cavity lengths of 0.1-1 cm. For a 2 cm long cavity Raman threshold can not be reached. Again, like in the previous case a

cavity with length of 0.5-1 cm is more stable against variation of coupling reflectivity than the 0.1 cm long cavity.
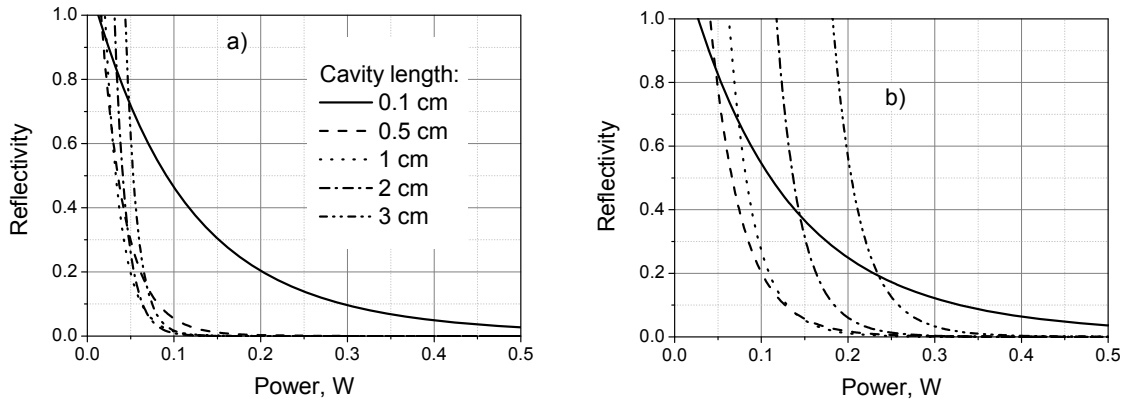

Figure II.2.2.4: Dependence of reflectivity for coupling at Stokes wavelength, which is required to achieve Raman threshold, on pump power inside of the cavity of the Raman ring laser. The dependencies were calculated for different lengths of cavity and for the following parameters of the cavity: g = 80 cm/GW, α = 5 dB/cm (a) and α = 10 dB/cm (b), t_{FC} = 0.3 ns.
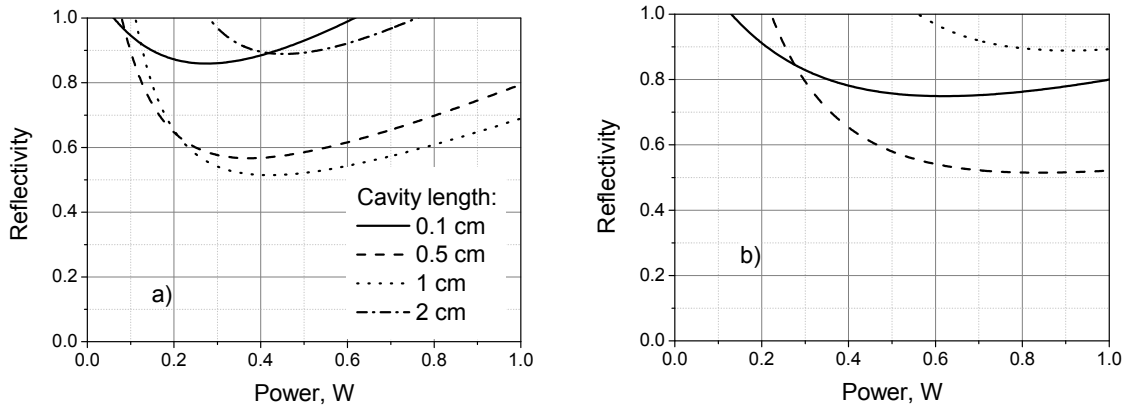

Figure II.2.2.5: Dependence of reflectivity for coupling at Stokes wavelength, which is required to get Raman threshold, on pump power inside of the cavity of the Raman ring laser. The dependencies were calculated for different lengths of cavity and for the following parameters of cavity: g = 20 cm/GW, α = 5 dB/cm, t_{FC} = 1 ns (a) and α = 10 dB/cm, t_{FC} = 0.5 ns (b).

Thus, for almost all above considered cases optimum cavity length is 0.5-1 cm. The coupling region should provide a reflectivity at Stokes wavelength of about 0.9-0.8. This value of reflectivity provides Raman operation in the ring laser even in the case of a low value of Raman gain coefficient (see Figure II.2.2.5).

Another important parameter that should be optimized is coupling reflectivity (or transmittance) at pump wavelength. The pump power inside of the cavity of the Raman laser depends on the value of pump power in the input waveguide as follows [7]:

$$P_{Inc} = P_P(0) \frac{\left(1 - \sqrt{\dfrac{P_P(L_{CR})}{P_P(0)} \cdot (1 - K_P)}\right)^2}{K_P}, \tag{65}$$

where $P_P(z)$ is the distribution of pump power along the cavity length, K_P is the transmittance of the coupling region at pump wavelength, P_{Inc} is the pump power in the input waveguide.
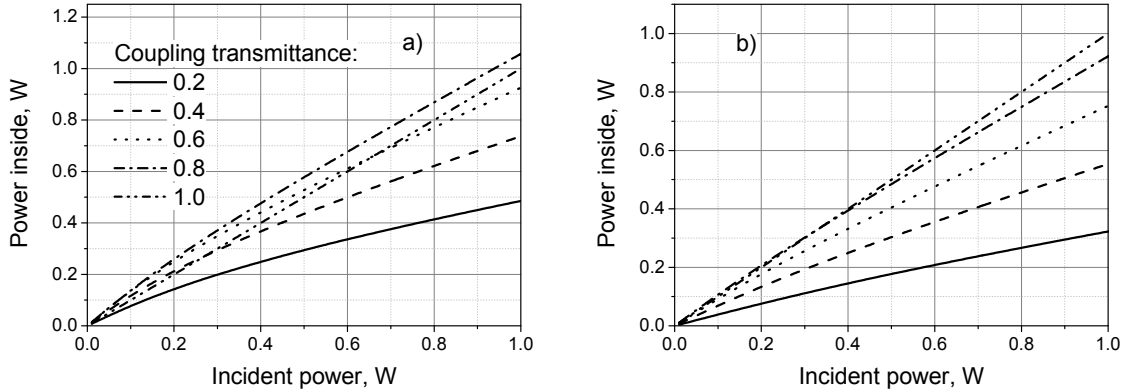

Figure II.2.2.6: Dependencies of pump power inside of the cavity on input pump power. The dependencies were calculated for a cavity length of 1 cm and for following values of propagation losses and free-carrier time: α = 5 dB/cm, t_{FC} = 0.3 ns (a) and α = 10 dB/cm, t_{FC} = 1 ns (b).
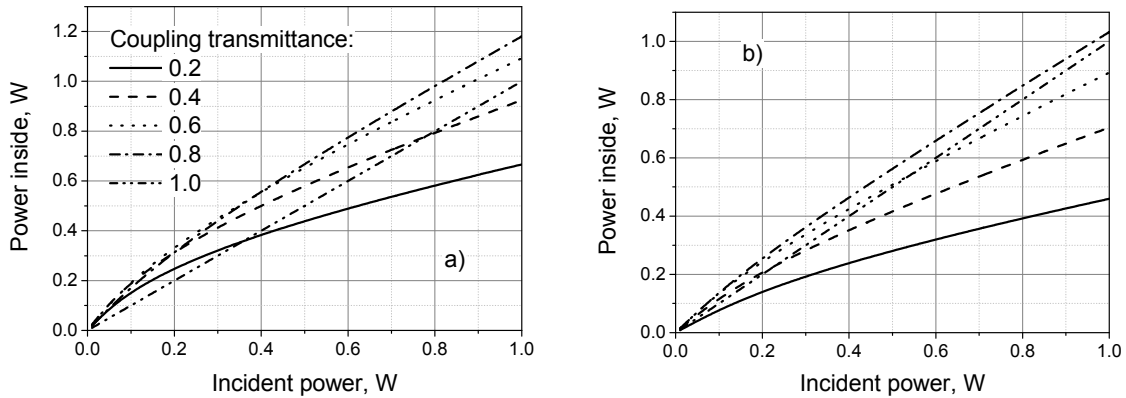

Figure II.2.2.7: Dependencies of pump power inside of the cavity on input pump power. The dependencies were calculated for a cavity length of 0.5 cm and for the following values of propagation losses and free-carrier time: α = 5 dB/cm, t_{FC} = 0.3 ns (a) and α = 10 dB/cm, t_{FC} = 1 ns (b).

It can be seen from (65) that optimal coupling depends on the ratio $P_P(L_{CR})/P_P(0)$, which is the decrease of pump power during one-pass through the cavity. Figures II.2.2.6 and II.2.2.7 present the dependencies of pump power $P_P(0)$ inside of the cavity at the beginning, on input pump power (P_{Inc}) calculated for a cavity length of

1 cm (Figure II.2.2.6) and 0.5 cm (Figure II.2.2.7), respectively, and for different values of propagation losses and free-carriers time. It can be seen that for almost all considered cases the coupling transmittance should be 0.8. Only for the case of the long cavity (1 cm) and high propagation losses (10 dB/cm) the coupling transmittance should be equal to 1. Thus, the coupling transmittance should be in the range 0.8-1. These values provide the highest value of pump power in the cavity.

II.3 High frequency electric-impedance of SOI elements and connectors

An important role in creation of fast electro-optical modulators is played by proper design of electrical contacts. They should have a high transmission band to provide a propagation of fast electrical signal. Also contacts should be coupled with usual coaxial electrical cables with impedance of 50 Ohm. Such design and impedance calculation were made by TH WIldau.

Typically, the integrated electrical elements are connected with the coaxial cable with the help of thin parallel gold or copper wires. Often, this short part of the scheme is neglected in calculations of impedance. But, as a possible source of distortion it should be taken into account. In case of parallel wire line one can obtain impedance as[21]:

$$Z = \frac{Z_0}{\pi\sqrt{\varepsilon_r}} arc\cosh\left(\frac{D}{d}\right) \tag{66}$$

where Z_0 is the impedance of free space (approximately 377 Ω), ε_r is the effective dielectric constant (which for air is 1.00054). If the separation D is much greater than the wire diameter d then this is approximately

$$Z_0 = \frac{276}{\sqrt{k}}\log\frac{d}{r} \tag{67}$$

In case, when wires with diameter 100 μm are used one has:
  r=100 μm
  d=5 mm
  Z_0=469 Ohm

As can be seen, the value of 469 Ohm is about 10 times higher than a typical impedance of a coaxial cable (50 Ohm).

$$Z_0 = \frac{276}{\sqrt{k}} \log \frac{d}{r}$$

Where,

Z_0 = Characteristic impedance of line
d = Distance between conductor centers
r = Conductor radius
k = Relative permittivity of insulation
     between conductors

Figure II.3.1: The parallel wire line and formula for calculation of impedance.

     As recommendation, the distance between wires must be as short as possible. For instance, reducing the distance length to 2 mm provides a decrease of line impedance to ~150 Ohm. For the required impedance of 50 Ohm the distance between wires must be around 150 µm.
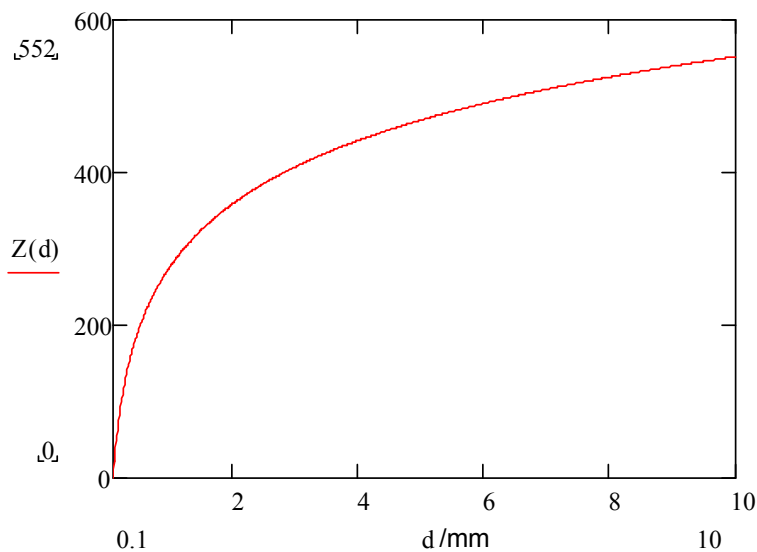

Figure II.3.2: Impedance of the parallel wire line versus length of the line. Short lengths tend to lower values of impedance. The graph is calculated for a wire radius of 100 µm and a distance between wires of 5 mm.

The conductor backed coplanar waveguide (see Figure II.3.3) provides a lower electromagnetic interference radiation compared to common microstrip lines or coplanar waveguides.
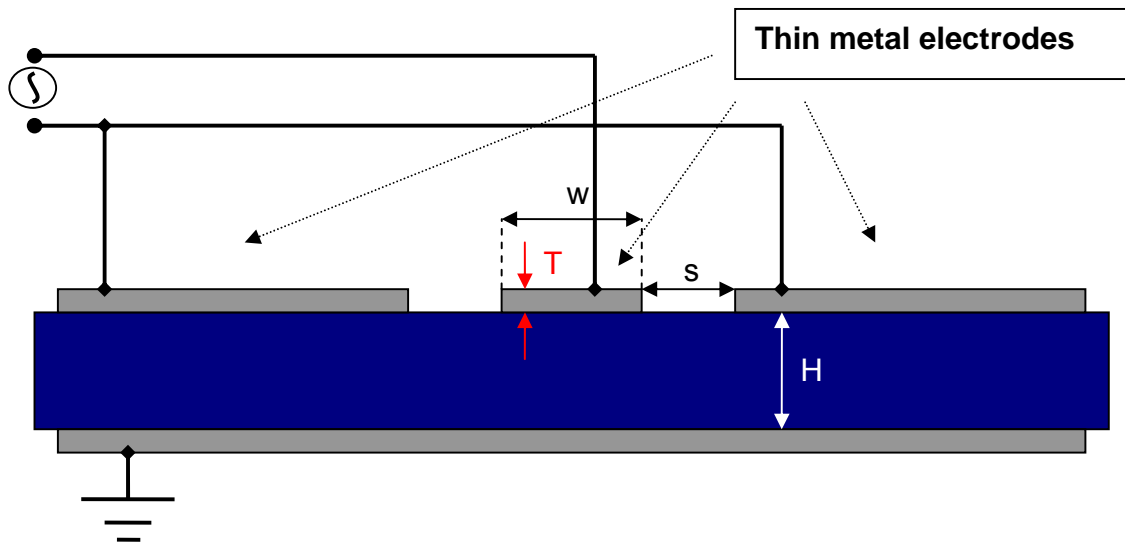
Figure II.3.3: Cross-section through a conductor backed coplanar waveguide. The geometrical parameters were optimized to be w=80 µm, s= 80 µm, T=0.58 µm, H=1.64 µm.

The most important feature of this type of structure is that the signal line and ground planes are all placed on one side, typically the upper side, of the substrate. But, compared to usual coplanar waveguides the values of phase constant and impedance can be changed as a result of the barrier existence. Therefore, an electromagnetic simulation is essential to obtain these values. The demonstrator works at high frequency of modulation (≥ 10 GHz). For optimal energy transfer from an external source to the active area the device (modulator) and the cable must be matched. This means both impedances must be equivalent.

The input impedance is calculated as usual as the ratio between applied voltage and actually flowing current. For an infinite line the impedance can be calculated analytically. The general expression for the characteristic impedance Z_0 of a transmission line is [22, 23]:

$$Z_0 = \sqrt{\frac{R + j\omega L}{G + j\omega C}} \qquad (68)$$

where R is the resistance per unit length, L is the inductance per unit length, G is the conductance of the dielectric per unit length, C is the capacitance per unit length, j is the imaginary unit, and ω is the angular frequency.

In our case using SiO_2 as insulator and gold as conductive electrode material one can assume that R and G are both zero. For such lossless line, the equation for the characteristic impedance reduces to

$$Z_0 = \sqrt{\frac{L}{C}} \tag{69}$$

The imaginary term j has also been canceled out, making Z_0 a real expression, being purely resistive.

As seen on Figure II.3.4: the electrical connection used in the demonstrator is a conductor backed coplanar waveguide, but in the area near to the waveguide its planar geometry changes. In this case the numerical calculation is preferable. In TH Wildau the integrated structure was analyzed by means of finite elements analysis. For simulation the commercial software COMSOL Multiphysics® was used.

The configuration of electrodes was optimized to have approximately 50 Ohm of impedance to be matched with standard coaxial cables. According to the calculations the electrodes provide an impedance of 47.1 Ohm at 10 GHz.
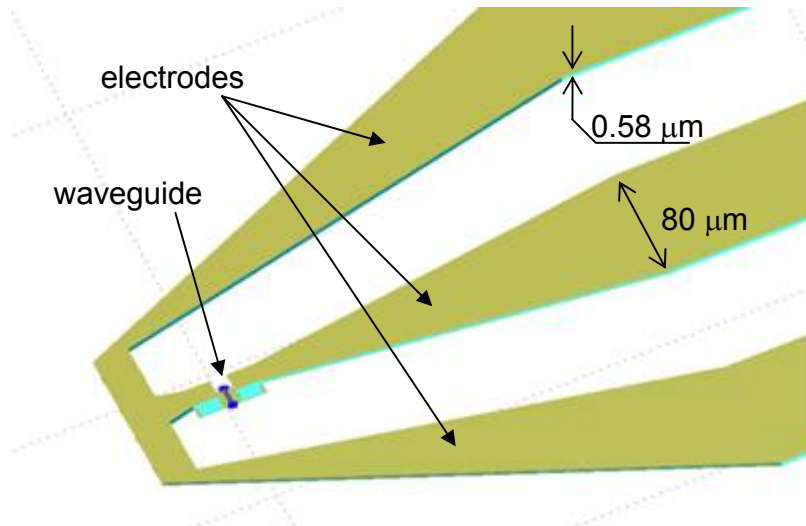

Figure II.3.4: 3D sketch of the electrical connection of the SOI optical element. Lower (ground) electrode is not shown.

II.4 Investigation of electro-optical polymers (fabrication, poling, and testing)

One of the project tasks was a development of technology of fabrication and poling of polymer materials for the use in electro-optical modulators based on plane Fabry-Perot resonators. For carrying out of this task a synthesis of a set of polymers and chromophores for doping of these polymers was developed.

II.4.1 Chromophores

For activation a polymer should be doped with a chormophore. For this purpose new azo- and azomethin-chromophpres with high stability were synthesized. Azochromophores were produced by diazotization of aromatic amines (aniline derivatives) and subsequent reaction of diazonium salts with phenol or phenol derivatives. The following reaction equation shows an example of reaction for p-trifluormethyl-perfluoranilin and benzol

$$CF_3-C_6F_4-NH_2 \xrightarrow{NaNO_2/H_2SO_4} \xrightarrow[]{/ NaOH} CF_3-C_6F_4-N=N-C_6H_4-OH$$
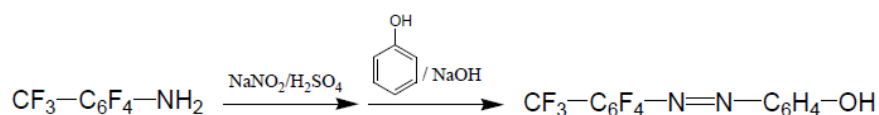
Azomethinchromophores were produced by condensation of aromatic aldehydes with aromatic amines. The following equation shows as an example the reaction of p-trifluoromethyl-benzaldehyde with p-Dimethylaminoanilin:

$$CF_3-C_6F_4-CHO + H_2N-C_6H_4-N(CH_3)_2 \xrightarrow{Ethanol}$$

$$CF_3-C_6F_4-CH=N-C_6H_4-N(CH_3)_2$$
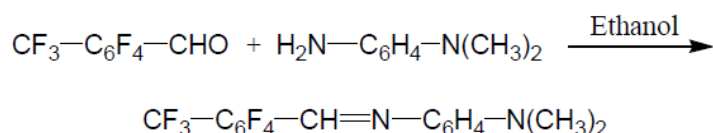
After the reaction all chromophores were purified by column chromatography in silica gel with methylene chloride as eluent and then reprecipitated from n-Heptan/Methylenchlorid. The resulting products were analytically characterized (thin layer chromatography, IR spectroscopy, elemental analysis).

II.4.2 Polymers

The following polymers were used for host-guest systems (chromophores physically embedded in polymer matrix): Polyphenylchinoxalin IIB (PPQ IIB) from own synthesis, polycarbonate (PC), poly (1-methoxy-4-O-dispersrot 1) -2,5-bis (2-metoxyethyl) benzene, and poly (methyl acrylate dispersrot 1)] (see Figure II.4.2.1), which is commercially available.

PPQ IIB

PC

Poly(1-methoxy-4-O-dispersrot 1)-
2,5-bis(2-metoxyethyl)benzen

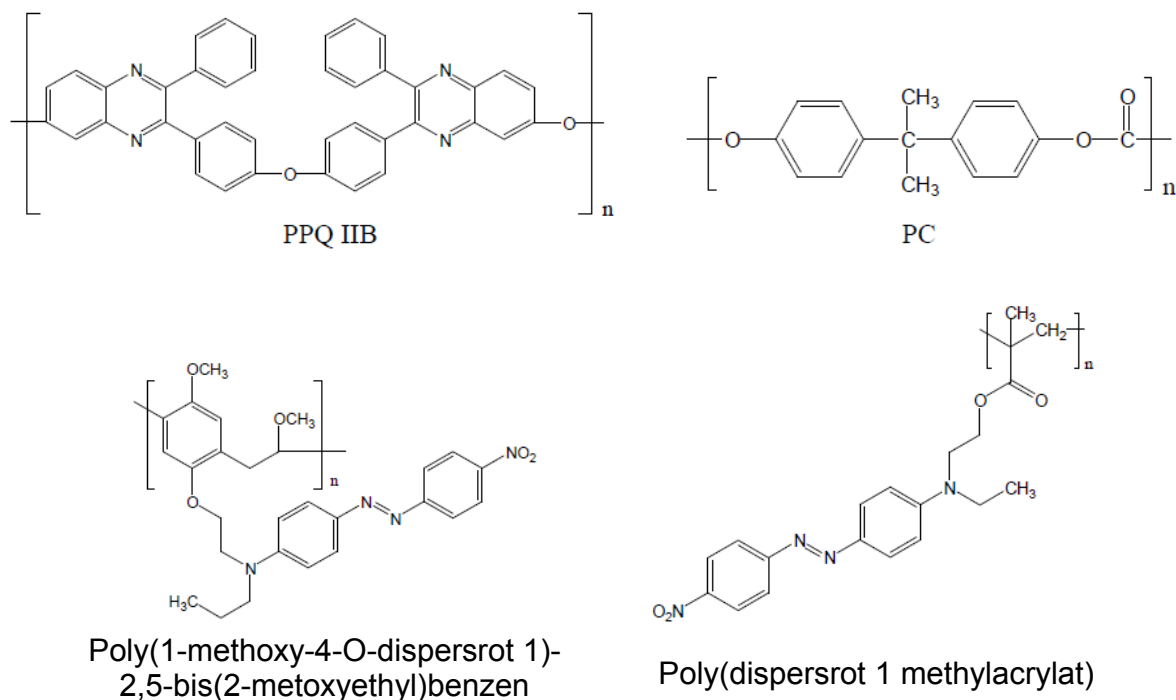Poly(dispersrot 1 methylacrylat)

Figure II.4.2.1: Structure of PPQ IIB and PC polymers.

In addition a matrix polymer and two side-chain polymers (polyamide) were synthesized, where the chromophore is covalently bound to the polymer chain.

II.4.3. Characterization

For the characterization of polymers and for development of methods of their production prism-coupling as well as profilometer were used. Using prism-coupling the dependencies of refractive index for TE and TM-waves on concentration of chromophore and on light wavelength were determined. The typical dependencies are presented in Tables II.4.3.1 and II.4.3.2.

Table II.4.3.1: Dependence of refractive index of PC with disperse red 1 (DR1) on concentration of DR1. Light wavelengths is 1064 nm

Concentration of DR1, wt%	Refractive index for TE wave	Refractive index for TM wave
0.5	1.5705	1.5691
1	1.5712	1.5698
2	1.5736	1.5706

3	1.5755	1.5698
5	1.5780	1.5693

Table II.4.3.2: Dependence of refractive index of PPQ IIB with own synthesized chromophore (UAS 12, 2.1 wt%) on light wavelength

Wavelength, nm	Refractive index for TE wave	Refractive index for TM wave
632.	1.7411	1.6988
830	1.7197	1.6695
980	1.7103	1.6612

Measurements with profilometer gave the dependencies of polymer layer thickness on spin-coater rotation speed and acceleration. Typical dependence of layer thickness on rotation speed is presented in Figure II.4.3.1 for polycarbonate with DR1 (0.5 wt%) on glass substrate.
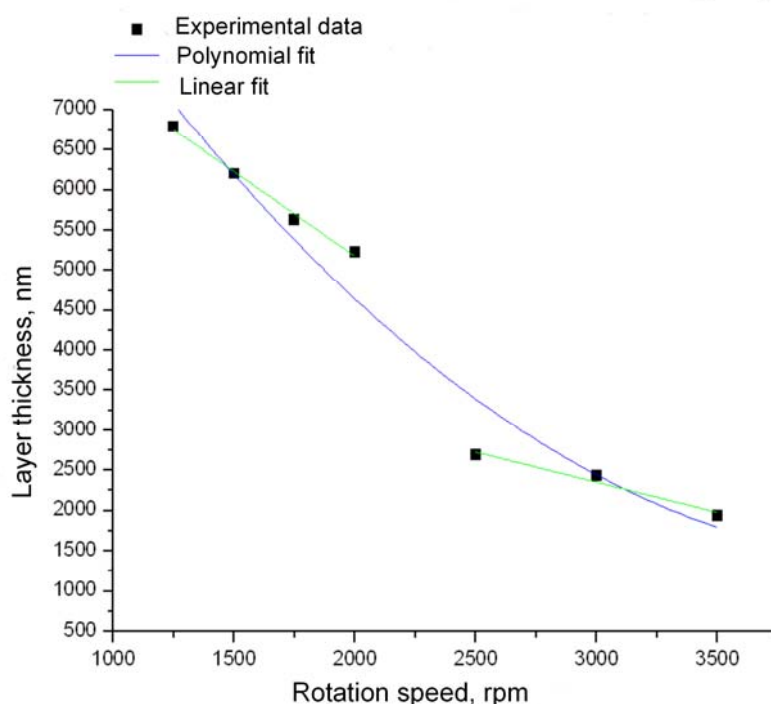

Figure II.4.3.1: Dependence of layer thickness on rotation speed of spin-coater. Material is PC with DR1 (0.5 wt%) on glass substrate.

To provide second-order nonlinear properties for polymer layers with chromophores these chromophores were oriented using poling. For this purpose corona poling was used. Samples were heated up to temperature of 160°C, which is slightly

higher than the glass temperature (about 148°C for polycarbonate). Then the samples were polarized during 15 min using corona discharge with limiting current of 20 µA and voltage of 6-8 kV. Finally samples were cooled down to room temperature with an applied voltage.

After poling samples were analyzed for their transmission. This allows us to measure relaxation of the chromophore molecules. The measurements were carried out both immediately after poling (after several minutes or hours) and in the long time (after some days or weeks). Dependence of change of transmission of PC doped with DR1 on DR1 concentration is seen in Figure II.4.3.2, while the relaxation of this change in time for a sample with DR1 concentration of 3 wt% is demonstrated in Figure II.4.3.3.
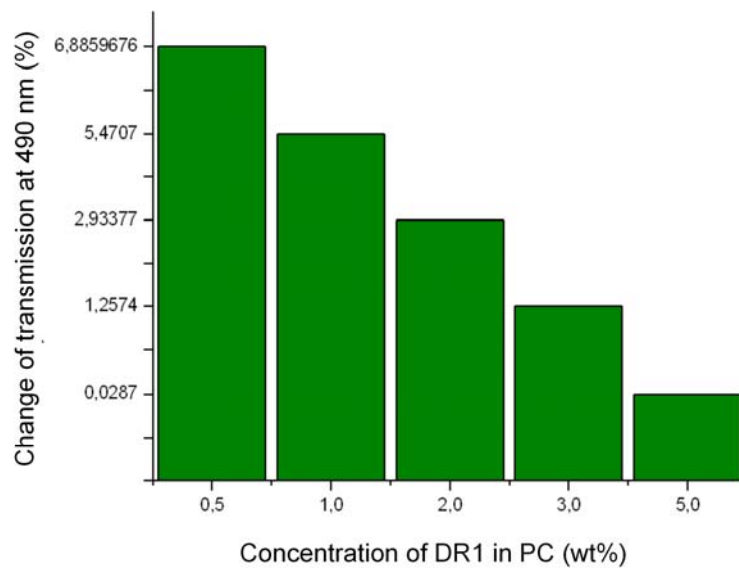

Figure II.4.3.2: Dependence of change of transmission of PC doped with DR1 at wavelength of 490 nm on DR1 concentration.

Chromophore orientation provided with corona poling increases second-order nonlinearity of polymer layers required for electro-optical modulation. This is shown in Figure II.4.3.4, where results of second harmonic test are presented. This figure shows second harmonic signal provided by indium tin oxide (ITO) layer, by non-poled polymer PPQ IIB layer coated on the ITO layer, and by this polymer layer after poling. It can be seen, that second harmonic signal after poling procedure is sufficiently higher than that before.
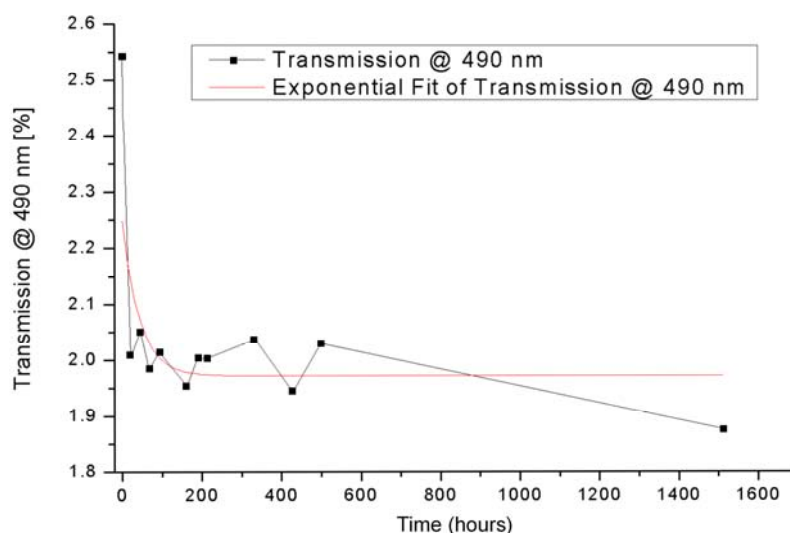
Figure II.4.3.3: Time relaxation of change of transmission of PC doped with DR1 (3 wt%).
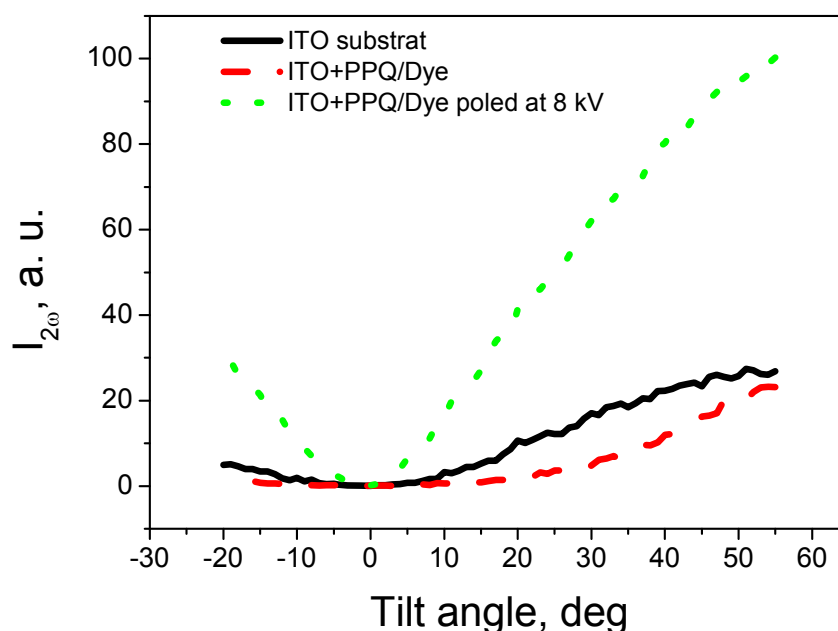

Figure II.4.3.4: Intensity of second harmonic signal as a function of angle of incidence on samples of PPQ IIB doped with chromophore 2-{2-[2-(4-Dimethylamino-phenyl)-vinyl]-chromen-4-ylidene}-malonitrile.

In addition, thermal stability of polymer layers was investigated. The thermal stability plays an important role for long-term stability of the components to be developed. The thermal behavior of produced polymer layers was investigated using differential scanning calorimetry (DSC). It should be noted that obtained data for thermal behavior are also important for determination of poling temperature. As an example DSC

data for pure PC sample and PC doped with DR1 are presented in Figure II.4.3.5. It is seen that pure PC has a glass transition temperature of 148°C, while the presence of DR1 reduces this temperature significantly (down to 69°C).
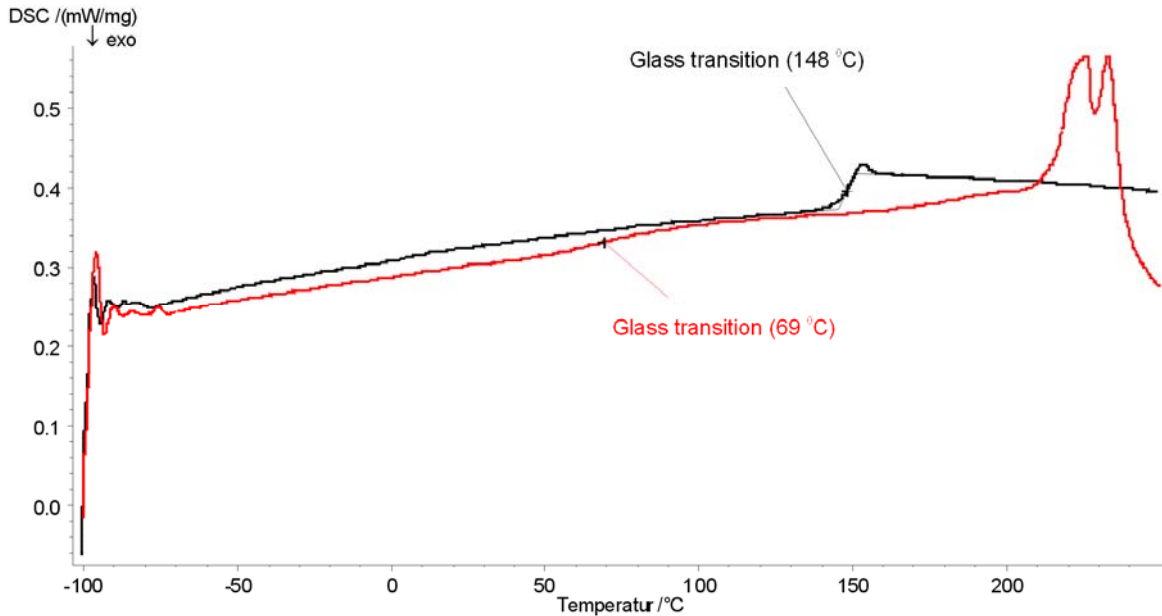

Figure II.4.3.5: DSC for pure PC (black line) and PC with DR1 (5 wt%) (red line). Heat rate was 10°C/min.

The results obtained during investigation of polymer layers were transferred to the project partner TUB for design of modulators at the base of these layers.

In summary it could be achieved that layers of high optical quality can be produced by means of chromophore doped polymer guest host systems. The best layers were obtained from doped polycarbonate. However, depending on doping level a reduction of glass transition temperature is observed. This means that for long-term stable systems only low doping levels are appropriate. Doped PPQ shows also a reduction of glass transition temperature by doping but can in principle also be used for applications in EO modulators.

Application of multilayer Bragg mirrors to the polymer systems caused some surface modification by structural relaxation of the polymer. This problem could not be used during project duration but is still under investigation. The solution might be a further reduction of heat formation while the multilayers are deposited onto the polymer surfaces. This work is important to be continued in order to obtain EO modulators with small spatial foot-print which are able to reach modulation frequencies in the range above 40 GHz.

Publications

The scientific results obtained during the project were presented in the following publications:

1. Stimulated Raman scattering and Raman lasing in bulk silicon at low temperatures, Hanjo Rhee, Oliver Lux, Stefan Meister, Victor A. Lisinetskii, Ulrike Woggon, Alexander A. Kaminskii, and Hans J. Eichler, Applied Physics B, (in preparation).
2. Investigation of room-temperature Raman conversion in bulk-silicon, Victor Lisinetskii, Sigurd Schrader, Optics Communications (in preparation)
3. Sinusoidal width modulated micro-cavities in SOI waveguides, Stefan Meister, Aws Al-Saadi, Bülent A. Franke, Sebastian Kupijai, Lars Zimmermann, Harald H. Richter, Bernd Tillack, Sigurd K. Schrader, Ulrike Woggon, and Hans J. Eichler, Optics Express, (in preparation).
4. Spontaneous and stimulated Raman scattering in planar silicon waveguides, Sha Wang, Stefan Meister, Shaimaa Mahdi, Bülent Franke, Aws Al-Saadi, Lars Zimmermann, Harald H. Richter, David Stolarek, Viktor Lisinetskii, Sigurd K. Schrader, Hans Eichler, Silicon Photonics VI, Proceedings of SPIE, 7943, 7943-40, (2011).
5. Photonic crystal microcavities in SOI waveguides produced in a CMOS environment, S. Meister, B. A. Franke, S. Mahdi, A. Al-Saadi, B. Kuhlow, K. Voigt, B. Tillack, H. H. Richter, L. Zimmermann, S. Schrader, V. Ksianzou, H. J. Eichler, Silicon Photonics V, Proceedings of SPIE, 7606, 7606-41, (2010).
6. Investigation of Raman threshold conditions in bulk silicon, V. Lisinetskii H. Rhee, S. Schrader, H.J. Eichler, EOS Annual Meeting 2010, - 29 October 2010, Paris, France, TOM 6: Nonlinear Optics and Photonics, Digest on CD.
7. Operation of Raman laser based on silicon bulk-crystal at temperature of 10 K, V. Lisinetskii, O. Lux, H. Rhee, S. Schrader, H.J. Eichler, EOS Topical Meetings at Capri 2011, Italy, 26 - 28 September 2011, 2nd EOS Topical Meeting on Lasers ETML'11, Digest on CD.
8. Investigation of room-temperature Raman conversion in bulksilicon, V. Lisinetskii, S. Schrader, EOS Topical Meetings at Capri 2011, Italy, 26 - 28 September 2011, 4th EOS Topical Meeting on Optical Microsystems OµS'11, Digest on CD.
9. Investigation of Raman generation threshold in bulk silicon (*in Russian*), V.A. Lisinetskii, H. Rhee, S. Schrader, H.J. Eichler, VIII Internationnal conference "Laser physics and optical technology", Minsk , Belarus, 27-30 September 2010, Conference proceedings, vol.2, p.46-49.
10. Micro-cavities based on width modulated SOI waveguides, Stefan Meister, Aws Al-Saadi, Bülent A. Franke, Shaimaa Mahdi, Miroslaw Szczambura, Berndt Kuhlow, Ulrike Woggon, Lars Zimmermann, Harald H. Richter, David Stolarek, Sigurd K. Schrader, Hans J. Eichler, Silicon Photonics VI, Proceedings of SPIE, 7943, 7943-28, (2011).
11. Observation of spontaneous Raman scattering in 220nm Silicon-on-Insulator (SOI) waveguides, Shaimaa Mahdi, Sha Wang, Aws Al-Saadi, Bülent A. Franke, Viktor Lisinetskii, Sigurd Schrader, Stefan Meister, and Hans J. Eichler, DPG-Verhandlungen, Q 8.6, Dresden (2011).
12. Spontaneous and stimulated Raman scattering in planar silicon waveguides, Sha Wang, Stefan Meister, Shaimaa Mahdi, Bülent Franke, Aws Al-Saadi, Lars

Zimmermann, Harald H. Richter, David Stolarek, Viktor Lisinetskii, Sigurd K. Schrader, Hans Eichler, OPTO, Silicon Photonics VI, Photonics West, Paper 7943-40, San Francisco, CA, USA (2011).

13. Photonic crystal microcavities in SOI waveguides produced in a CMOS environment, S. Meister, B. A. Franke, S. Mahdi, A. Al-Saadi, B. Kuhlow, K. Voigt, B. Tillack, H. H. Richter, L. Zimmermann, S. Schrader, V. Ksianzou, H. J. Eichler, Photonics West 2010, OPTO, Silicon Photonics V, Paper 7606-41, San Francisco, CA, USA (2010).

14. Simulation analysis of one-dimensional photonic crystal Fabry-Perot filters, Aws Al-Saadi, Bülent A. Franke, Shaimaa Mahdi, Sigurd Schrader, Viachaslau Ksianzou, Harald Richter, Stefan Meister, and Hans J. Eichler, DPG-Verhandlungen, Q 60.4, Hannover (2010).

15. Fabry-Perot microcavities in ultra-small SOI waveguides, Bülent A. Franke, Aws Al-Saadi, Shaimaa Mahdi, Sigurd Schrader, Viachaslau Ksianzou, Harald Richter, Stefan Meister, and Hans J. Eichler, DPG-Verhandlungen, Q 67.4, Hannover (2010).

16. Micro-cavities based on width modulated SOI waveguides, Stefan Meister, Aws Al-Saadi, Bülent A. Franke, Shaimaa Mahdi, Miroslaw Szczambura, Berndt Kuhlow, Ulrike Woggon, Lars Zimmermann, Harald H. Richter, David Stolarek, Sigurd K. Schrader, Hans J. Eichler, OPTO, Silicon Photonics VI, Photonics West, Paper 7943-28, San Francisco, CA, USA (2011).

17. SiO_2 coated 1D-photonic crystal microcavities in ultra-small SOI waveguides, Sebastian Kupijai, Bülent A. Franke, Aws Al-Saadi, Miroslaw Szczambura, Shaimaa Mahdi, Viachaslau Ksiandzou, Sigurd Schrader, Hans J. Eichler, and Stefan Meister, DPG-Verhandlungen, Q 590, Dresden (2011).

18. Simulation and design of electro-optic modulator based on SOI waveguides, Aws Al-Saadi, Bülent A. Franke, Shaimaa Mahdi, Miroslaw Szczambura, Viachaslau Ksiandzou, Sigurd K. Schrader, Stefan Meister, and Hans J. Eichler, DPG-Verhandlungen, Dresden (2011).

Literature

1.   Ralston, J.M. and R.K. Chang, *Spontaneous-Raman-scattering efficiency and stimulated scattering in silicon.* Physical Review B, 1970. **2**(6): p. 1858-1862.

2.   Chandrasekharan, V., *Scattering matrix for Raman effect in cubic crystals.* Zeitschrift fьr Physik A Hadrons and Nuclei, 1963. **175**(1): p. 63-69.

3.   McMaster, W.H., *Matrix representation of polarization.* Reviews of Modern Physics, 1961. **33**(1): p. 8-28.

4.   De Leonardis, F., V. Dimastrodonato, and V.M.N. Passaro, *Modelling of a DBR laser based on Raman effect in a silicon-on-insulator rib waveguide.* Semiconductor Science and Technology, 2008. **23**(6): p. 64008_1-64008_10.

5.   Rukhlenko, I.D., et al., *Continuous-wave Raman amplification in silicon waveguides: beyond the undepleted pump approximation.* Optics letters, 2009. **34**(4): p. 536-538.

6.   De Leonardis, F. and V.M.N. Passaro, *Ultrafast Raman Pulses in SOI Optical Waveguides for Nonlinear Signal Processing.* IEEE Journal of Selected Topics in Quantum Electronics, 2008. **14**(3): p. 739-751.

7.   Rong, H., et al., *Monolithic integrated Raman silicon laser.* Optics Express, 2006. **14**(15): p. 6705-6712.

8.   Claps, R., et al., *Influence of nonlinear absorption on Raman amplification in Silicon waveguides.* Optics Express, 2004. **12**(12): p. 2774-2780.

9.   Rong, H., et al., *An all-silicon Raman laser.* Nature, 2005. **433**: p. 292-294.

10.   Jalali, B., et al., *Prospects for silicon mid-IR Raman lasers.* IEEE J. Sel. Top. Quantum Electron, 2006. **12**: p. 1618-1627.

11.   Jian-Wei, W.U., L.U.O. Feng-Guang, and G.C. de Mello, *High Speed Signal Wavelength Conversion Using Stimulated Raman Effect in Ultrasmall Silicon-on-Insulator Optical Waveguides.* Chinese Physics Letters, 2008. **25**(2): p. 574-577.

12.   Boyraz, O. and B. Jalali, *Demonstration of a silicon Raman laser.* Optics Express, 2004. **12**(21): p. 5269-5273.

13.   Duzy, C., et al., *Stokes wavefront preservation in broad-band forward raman amplification.* Quantum Electronics, IEEE Journal of, 1987. **23**(5): p. 569-574.

14.   Penzkofer, A., A. Laubereau, and W. Kaiser, *High intensity Raman interactions.* Prog. Quant. Electron., 1979. **6**: p. 55-140.

15.   Lisinetskii, V.A., et al., *Raman Gain Coefficient of Barium Nitrate Measured for the Spectral Region of TI:Sapphire Laser.* Journal of Nonlinear Optical Physics and Materials, 2005. **14**(01): p. 107-114.

16.   Hodgson, N. and H. Weber, *Laser Resonators and Beam Propagation. Fundamentals, Advanced Concepts and Applications.* second ed. 2005, New York: Springer Science+Business Media, Inc. 653.

17.   Comsol, A., *COMSOL multiphysics user's guide.* Version: September, 2005.

18.   Yuan, G., *Characterization of integrated optical waveguide devices.* 2008: ProQuest.

19.   Jackson, J.D. and R.F. Fox, *Classical electrodynamics.* American Journal of Physics, 1999. **67**: p. 841.

20.   Dimitropoulos, D., et al., *Lifetime of photogenerated carriers in silicon-on-insulator rib waveguides.* Applied Physics Letters, 2005. **86**: p. 071115.

21.   Balanis, C.A., *Antenna theory: analysis and design.* 1982: Harper & Row New York.

22.   Tien, C.C., et al., *Transmission characteristics of finite-width conductor-backed coplanar waveguide.* Microwave Theory and Techniques, IEEE Transactions on, 1993. **41**(9): p. 1616-1624.

23.   Simons, R.N. and Simons, *Coplanar waveguide circuits, components, and systems.* 2001: Wiley Online Library.